Clim Dyn
DOI 10.1007/s00382-012-1506-x

Control of deep convection by sub-cloud lifting processes: the ALP closure in the LMDZ5B general circulation model

Catherine Rio · Jean-Yves Grandpeix · Frédéric Hourdin · Francoise Guichard · Fleur Couvreux · Jean-Philippe Lafore · Ann Fridlind · Agnieszka Mrowiec · Romain Roehrig · Nicolas Rochetin · Marie-Pierre Lefebvre · Abderrahmane Idelkadi

Received: 15 November 2011 / Accepted: 13 August 2012

Abstract Recently, a new conceptual framework for deep convection scheme triggering and closure has been developed and implemented in the LMDZ5B general circulation model, based on the idea that deep convection is controlled by sub-cloud lifting processes. Such processes include boundary-layer thermals and evaporatively-driven cold pools (wakes), which provide an available lifting energy that is compared to the convective inhibition to trigger deep convection, and an available lifting power (ALP) at cloud base, which is used to compute the convective mass flux assuming the updraft vertical velocity at the level of free convection. While the ALP closure was shown to delay the local hour of maximum precipitation over land in better agreement with observations, it results in an underestimation of the convection intensity over the tropical ocean both in the 1D and 3D configurations of the model. The specification of the updraft vertical velocity at the level of free convection appears to be a key aspect of the closure formulation, as it is weaker over tropical ocean than over land and weaker in moist mid-latitudes than semi-arid regions. We propose a formulation making this velocity increase with the level of free convection, so that the ALP closure is adapted to various environments. Cloud-resolving model simulations of observed oceanic and continental case studies are used to evaluate the representation of lifting processes and test the assumptions at the basis of the ALP closure formulation. Results favor closures based on the lifting power of sub-grid sub-cloud processes rather than those involving quasi-equilibrium with the large-scale environment. The new version of the model including boundary-layer thermals and cold pools coupled together with the deep convection scheme via the ALP closure significantly improves the representation of various observed case studies in 1D mode. It also substantially modifies precipitation patterns in the full 3D version of the model, including seasonal means, diurnal cycle and intraseasonal variability.

Keywords Deep convection parameterization · Triggering and closure · Oceanic versus continental convection · Diurnal cycle of precipitation · High resolution simulations to evaluate parameterizations assumptions

This paper is a contribution to the special issue on the IPSL and CNRM global climate and Earth System Models, both developed in France and contributing to the 5th coupled model intercomparison project.

C. Rio (✉)
Laboratoire de Météorologie Dynamique, CNRS/IPSL, UPMC, Tr 45-55, 3e et, B99 Jussieu, 75005 Paris, France
e-mail: catherine.rio@lmd.jussieu.fr

J.-Y. Grandpeix · F. Hourdin · R. Roehrig · N. Rochetin · A. Idelkadi
LMD, Paris, France

F. Guichard · F. Couvreux · J.-P. Lafore
Centre National de la Recherche Météorologique (CNRM/GAME), Toulouse, France

A. Fridlind · A. Mrowiec
Goddard Institute for Space Studies, NASA/GISS, New York, USA

M.-P. Lefebvre
LMD/CNRM, Paris, France

1 Introduction

The impact of parameterized convection on the large-scale circulation relies strongly on the condition used to activate

Published online: 13 September 2012

the deep convection scheme, called the triggering function, and on the closure of the system of equations that yields the convection intensity at the cloud base. The triggering function often involves the so-called "convective inhibition" (CIN), defined as the work of buoyancy forces in the region of negative buoyancy around the cloud base that an ascending parcel must overcome to reach its level of free convection (LFC). Regarding closures, observations sustaining a quasi-equilibrium between cumulus convection and the large-scale environment have led to the development of approaches relating convection intensity to large-scale variables involving an adjustment time (Arakawa and Schubert 1974; Arakawa and Chen 1987). This is the case, for example, of closures relying on the so-called "convective available potential energy" (CAPE, Emanuel 1991), defined as the work of positive buoyancy forces above cloud base (Moncrieff and Miller 1976). However, departures from the quasi-equilibrium are achieved when the variation of the forcing becomes comparable to the deep convection adjustment time, such as in presence of mesoscale organization, and when the forcing period becomes less than a few tens of hours, which is the case for diurnal variations (Donner and Phillips 2003; Jones and Randall 2011). From a climate perspective, such closures may not be the best suited as quasi-equilibrium, when achieved, should likely result from closure specification rather than being a model input (Del Genio and Yao 1993). Some studies propose closures based on large-scale horizontal moisture convergence (Tiedtke 1989) or on large-scale profiles below cloud base (Emanuel and Zivkovic-Rothman 1999; Del Genio and Yao 1993). Mapes (2000) proposes a closure that involves convective inhibition and a typical updraft vertical velocity at cloud base. Bretherton et al. (2004) propose a similar closure for shallow convection where they define this vertical velocity from the parameterized sub-cloud turbulent kinetic energy, taking into account the role of sub-grid sub-cloud processes in shallow convection development.

This paper discusses a new concept for triggering and closure introduced in the LMDZ general circulation model, which relates deep convection occurrence and intensity to the lifting effect of sub-grid sub-cloud processes. This is done by introducing two quantities (Grandpeix and Lafore 2010): the available lifting energy (ALE) and available lifting power (ALP) provided at the base of deep convective towers by sub-cloud processes. Deep convection is active whenever the available lifting energy is sufficient to overcome the convective inhibition:

$$\mathrm{ALE} > |\mathrm{CIN}| \tag{1}$$

where ALE is defined as the maximum of the various sub-cloud process contributions. The convective power above inhibition is then equal to the lifting power provided at cloud base (ALP) reduced by the power used to overcome the inhibition and the power lost by dissipation, which can be scaled with the updraft vertical velocity at the level of free convection w_b. The convective mass flux at the level of free convection (LFC) then reads:

$$M_b = \frac{ALP}{[|CIN| + 2{w_b}^2]} \tag{2}$$

where w_b is a free parameter. Those new triggering and closure formulations are introduced in the Emanuel (1991) deep convection scheme used in LMDZ4 (Hourdin et al. 2006). Since the Emanuel (1991) scheme already has a CAPE closure (giving a cloud-base mass flux M_0), this is done by rescaling saturated mass fluxes and the precipitating downdraft cross section by M_b/M_0. So far, sub-cloud processes providing lifting for deep convection in LMDZ include boundary-layer thermals and cold pools. Indeed, shallow cumulus clouds precursor of deeper clouds are the saturated part of thermals initiated in the surface layer (LeMone and Pennell 1976). A parameterization of dry and cloudy boundary-layer thermals has been developed (Hourdin et al. 2002; Rio and Hourdin 2008; Rio et al. 2010), which provides an explicit representation of thermals and associated shallow cumulus clouds. The scheme is combined with a diffusive scheme based on a prognostic equation for the turbulent kinetic energy (Yamada 1983). Its coupling with the Emanuel (1991) deep convection scheme was motivated by the need to better represent the succession of the three convective regimes, namely dry, shallow and deep, involved in the diurnal cycle of convection over land (Guichard et al. 2004). Once deep convection is initiated, the evaporation of precipitation in unsaturated downdrafts leads to the development of pools of cold air under convective systems. These pools spread at the surface like density currents, lifting the air at their edges, and contributing to maintain deep convection and initiate new convective cells (Houze and Hobbs 1982). This phenomenon has been highlighted in many field campaigns since GATE in the 1970s (Zipser 1969; Houze 1977; Lima and Wilson 2008). However, only two parameterizations have been proposed and tested in single column models (Qian et al. 1998; Rozbicki et al. 1999; Grandpeix and Lafore 2010; Grandpeix et al. 2010), and they have never been taken into account in any operational forecast or climate models so far. The parameterization of Grandpeix and Lafore (2010) has been developed and tested in the LMDZ model. When it is active, each model grid-cell is separated into two environments: the convective region and the cold pool region. As temperature and moisture perturbations in cold pools are prognostic variables of the scheme, a memory effect is introduced in the deep convection scheme, which allows it to maintain deep convection even after stabilization of low-levels such as during the early evening and night.

The thermal plume and cold pool parameterizations have been tested independently and the parameters involved have been tuned in the 1D version of the LMDZ model on several case studies. The thermal plume model was evaluated on cases of shallow cumulus over land and ocean (Rio and Hourdin 2008). The cold pool parameterization coupled to the Emanuel (1991) scheme with ALP closure was evaluated on a case of squall-line propagation over the Sahel for which boundary-layer tendencies were prescribed, and on a maritime case study in the western Pacific (Grandpeix et al. 2010). However, some parameters related to the cold pool characteristics had to be changed from the continental to the oceanic case study (Grandpeix et al. 2010). The whole set of parameterizations including thermals, cold pools and convection with ALP closure was tested for the first time on a case of a diurnal cycle of mid-latitude continental convection (Guichard et al. 2004). It was shown in particular to successfully simulate the diurnal cycle of continental convection in the mid-latitudes (Rio et al. 2009), in contrast with the long-standing diurnal bias of climate simulations.

In a full GCM however, parameterizations have to be adapted to all situations encountered all over the globe, from mid-latitude continents to tropical ocean or semi-arid regions. In order to proceed from 1D case studies to full 3D simulations, the ALP closure had to be revisited. Indeed, when first implemented in the full 3D version of LMDZ, the set of parameterizations described in Rio et al. (2009) led to a strong underestimation of deep convection intensity over tropical ocean. Similar behavior was obtained in 1D case studies of tropical convection. Based on a series of sensitivity experiments that were conducted both in 1D and 3D configurations, this paper explores the contrasting factors that control deep convection over land and ocean and revisits the ALP closure in order to make it valid in diverse environments. The 1D simulations include a case of oceanic tropical convection and a case of continental convection over the Sahel and are evaluated against simulations in which convection and clouds are explicitly resolved, using a so-called large-eddy simulations (LES) code or cloud-resolving model (CRM). Results are analyzed in order to attribute model improvements or deficiencies either to the assumption that deep convection is controlled by sub-cloud processes or to the representation of those processes itself. As will be discussed in this paper, a key aspect of the ALP closure formulation relies on the specification of the vertical velocity at the level of free convection, which happens to be weaker for oceanic than continental convection or for mid-latitude than semi-arid environments. Making this vertical velocity dependent on environmental conditions finally permitted the implementation of the new set of parameterizations in the 3D version of the LMDZ general circulation model. This LMDZ5B version of the model (Hourdin et al, 2012, this issue), the atmospheric component of IPSL-CM5B coupled model, has then been used to perform climate simulations in the framework of CMIP5[1] (Taylor et al. 2012).

This paper is organized as follows. In Sect. 2, the ALP closure is described in greater details and its behavior contrasted over land and ocean, leading to the definition of a set of sensitivity experiments related to the ALP closure specification. Then, hypotheses at the basis of the ALP formulation as well as the representation of sub-cloud lifting processes are evaluated against LES and CRM on a case of tropical oceanic convection in Sect. 3 and on a case of convection in a semi-arid environment in Sect. 4. Section 5 presents results obtained in the full 3D version of the model, regarding precipitation average and variability. Conclusions are drawn in Sect. 6.

2 The ALP closure revisited

2.1 The available lifting power

Sub-cloud processes that provide a lifting power to deep convection include boundary-layer thermals (subscript th) and cold pools (subscript wk for wakes), so that $ALP = ALP_{th} + ALP_{wk}$. The same framework could be used to include additional lifting effects, as those of thermal breezes along orography slopes or land-sea contrasts.

The available lifting power at cloud base is defined as the flux of kinetic energy at the condensation level, and is related to the third-order moment of the vertical velocity at that level. The contribution of thermals is computed as:

$$ALP_{th} = k_{th}\rho\overline{w'^3}/2 \tag{3}$$

where k_{th} is the conversion efficiency parameter set to 0.5 (Rio et al. 2009) and $\overline{w'^3}$ is computed from the vertical velocity inside thermal plumes w_{th} and the fractional coverage of thermal plumes α_{th} computed by the thermal plume model (Rio and Hourdin 2008) following:

$$\overline{w'^3} = \frac{\alpha_{th}(1-2\alpha_{th})}{(1-\alpha_{th})^2} w_{th}^3 \tag{4}$$

The contribution of wakes is computed from the flux of kinetic energy of air in contact with cold pool edges moving at a velocity C_*:

$$ALP_{wk} = k_{wk}h_{wk}L_{wk}\rho C_*^3/2 \tag{5}$$

where k_{wk} is the lifting efficiency set to 0.25, h_{wk} is the height of the cold pool and L_{wk} its perimeter per surface unit (Grandpeix et al. 2010). C_* is computed as:

[1] The fifth phase of Coupled Model Intercomparison Project.

$$C_* = k_*\sqrt{(2WAPE)} = k_*\sqrt{-2g\int_0^{h_{wk}} \frac{\delta\theta_v}{\overline{\theta_v}}dz} \quad (6)$$

WAPE being the wake available potential energy computed from the integral of the virtual potential temperature contrast between cold pools and their environment $\delta\theta_v$. k_* is a tunable parameter set to 0.33 (Grandpeix and Lafore 2010).

2.2 Test of the original ALP closure over land and ocean

In this section, the behavior of the ALP closure is contrasted over land and ocean by running the 1D version of the LMDZ model on two different case studies. The continental case study is the one on which the new set of parameterizations was originally tested by Rio et al. (2009). It is a simple case meant to be typical of diurnal convection in the mid-latitudes when convection is driven by surface fluxes. It is idealized from observations collected by the Atmospheric Radiation Measurement (ARM) facilities on the Oklahoma site the 27th June 1997 (the EUROCS[2] case, Guichard et al. 2004), so that simulations are not directly comparable with observations. As a reference, we rather rely on a simulation performed with the MESO-NH non-hydrostatic model (Lafore et al. 1998) run with a 2-km horizontal resolution (Guichard et al. 2004). The oceanic case study was built from observations collected in the region of Darwin, Australia, from 18 January to 4 February 2006 in the framework of the Tropical Warm Pool—International Cloud Experiment (TWP-ICE), characterized by a succession of "active" versus "suppressed" regimes of convection (Xie et al. 2010). Even if the TWP-ICE case is forced by constant SST, the observationally driven forcing include the fact that the considered region is coastal. This may have some influence on deep convection behavior during the suppressed period. As a reference we utilize a cloud-resolving simulation performed with the Distributed Hydrodynamic-Aerosol-Radiation Model Application (DHARMA, Stevens et al. 2002; Ackerman et al. 2000) run over a domain of 176 × 176 km with a horizontal resolution of 900 m, a time-step of 10 s and cyclic boundary conditions. The simulation is fully described in Fridlind et al. (2012).

The 1D simulations are performed with a 5-min time-step and a 39-level vertical grid. Surface fluxes and radiation are prescribed for the continental case while the sea surface temperature is fixed to a constant value of 29° Celsius and the surface and radiation schemes are activated for the oceanic case. Two versions of the model are first considered. The SP version is the standard version of the model, described in Hourdin et al. (2006), with a diffusive approach for boundary-layer turbulence (Laval et al. 1981) and the version of the Emanuel (1991) deep convection scheme with a CAPE closure. It is compared with simulation WB1, which corresponds to the version of the model used by Rio et al. (2009) to simulate the diurnal cycle of continental convection on the EUROCS case study. This includes the thermal plume model, the cold pool parameterization and the version of Emanuel (1991) deep convection scheme with ALE triggering and ALP closure, with tunable parameters set to $k_{th} = 0.5$, $k_{wk} = 0.25$ and $w_b = 1$ m s^{-1}.

The diurnal cycle of precipitation simulated by simulations SP (dash black) and WB1 (red) on the EUROCS case is compared to MESO-NH (crosses) in Fig. 1. As already shown in Rio et al. (2009), the new version of the model with ALP closure greatly improves the representation of this diurnal cycle in comparison with the standard version of the model, by shifting precipitation onset from 10:00LT to 12:00LT and precipitation maximum from 12:00LT to 17:00LT in better agreement with the CRM simulation. Even if the intensity of precipitation is overestimated, it is still in the range of the ensemble of CRM results presented in Guichard et al. (2004).

The time evolution of observed precipitation during TWP-ICE is displayed in the top panel of Fig. 2 (stars). The strongest deep convective events took place on the 19th, 22nd and 23rd of January, while monsoon conditions were suppressed afterward, with less intense precipitation. Simulated precipitation is largely constrained by prescribed large-scale forcing, so that it is expected to remain close to observations in all model runs. In the GCM, the total precipitation is the sum of precipitation produced by the deep convection scheme and by the large-scale cloud scheme. This latter scheme is diagnostic and assumes a sub-grid log-normal distribution of the total water (Bony and Emanuel 2001) with a standard deviation proportional to the mean of total water [see Hourdin et al. (2012) in this issue for more details]. The partitioning between

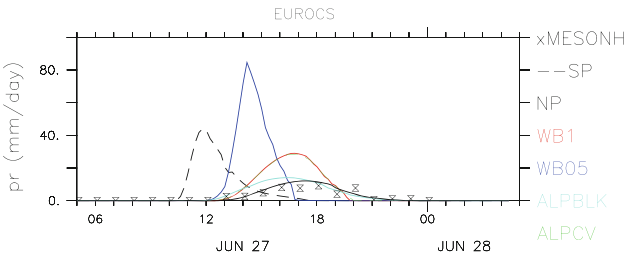

Fig. 1 Diurnal cycle of precipitation in the EUROCS case simulated with different versions of the LMDZ model in 1D mode: SP (*black dash*), NP (*black*), WB1 (*red*), WB05 (*blue*), ALPBLK (*light blue*), ALPCV (*green*), and compared with results from MESO-NH (*black crosses*)

[2] EUROpean Cloud Systems.

convective and large-scale precipitation is illustrated in the middle and bottom panels of Fig. 2, where the cumulative convective and large-scale precipitation over the whole period are shown. Results clearly show that the new set of parameterizations (simulation WB1, red line) yields less convective precipitation than the standard version of the model (simulation SP, black dash line). Since heating tendencies balance large-scale forcing over periods of several days over ocean, the decrease in the heating of the troposphere by the convection scheme in WB1 is compensated by an increase of large-scale condensation and associated precipitation. A textural algorithm (Steiner et al. 1995) is applied to 3-km radar reflectivity observations to distinguish convective from stratiform rain for qualitative comparison (black stars). During the active period, about 65 % of observed precipitation is convective, close to results shown in Varble et al. (2011) (their Table 3). It represents 61 % of total precipitation in simulation SP but only 13 % in simulation WB1.

The original formulation of the ALP closure presented and evaluated over land in Rio et al. (2009) succeeds to simulate the diurnal cycle of deep convection in the mid-latitudes, but tends to underestimate strongly deep convection intensity over tropical ocean.

2.3 Redefining the ALP closure formulation

Following Eq. 2, the mass flux at the base of convective towers is directly proportional to the available lifting power and inversely proportional to the inhibition and the vertical velocity specified at the level of free convection. Thus, convection intensity can be increased by either increasing the available lifting power or decreasing the power lost by dissipation by decreasing the vertical velocity at the level of free convection.

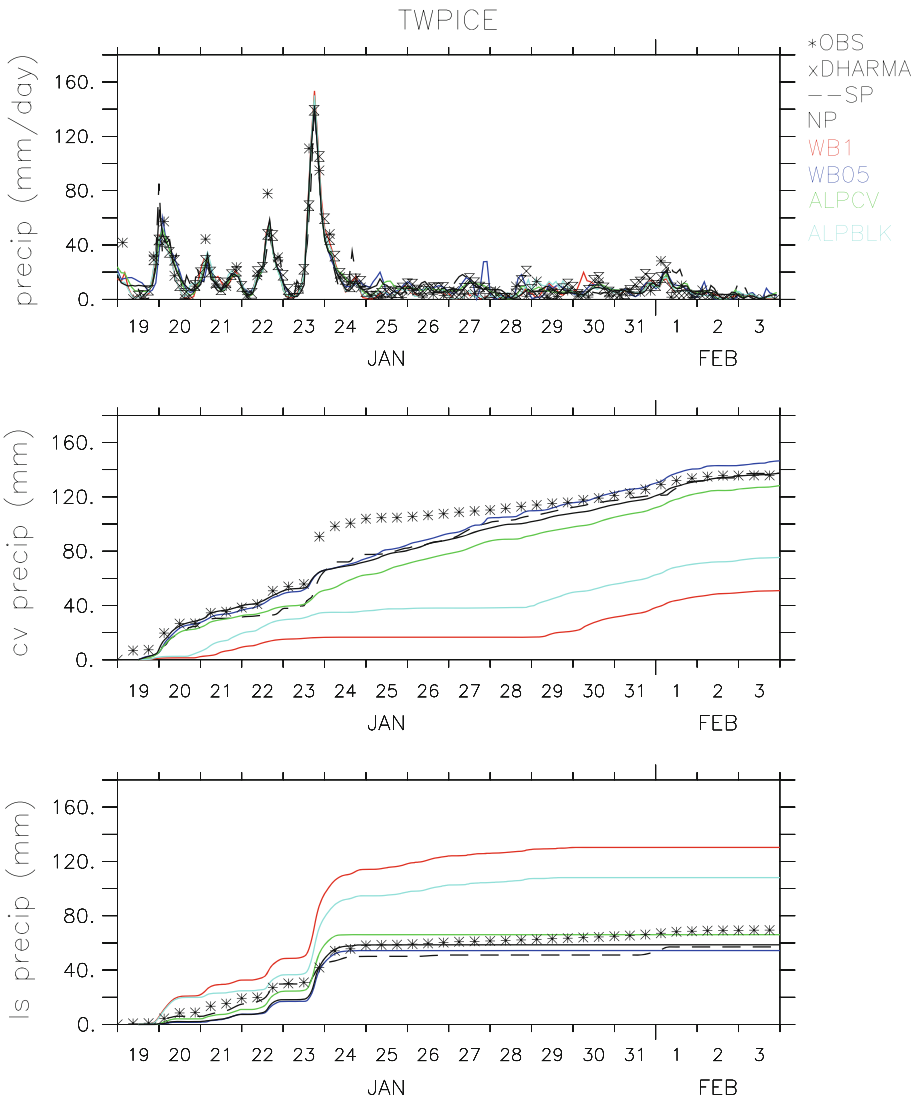

Fig. 2 Total precipitation (*top*), cumulative convective (*middle*) and large-scale (*bottom*) precipitation in the TWP-ICE case simulated with different versions of the LMDZ model in 1D mode: SP (*black dash*), NP (*black*), WB1 (*red*), WB05 (*blue*), ALPBLK (*light blue*), ALPCV (*green*). Total precipitation is compared with observations (*black crosses*) and DHARMA CRM (*black stars*). The Steiner et al. (1995) algorithm is applied to TWP-ICE observations to partition total precipitation into convective and stratiform

The available lifting power can be increased via the conversion-efficiency parameter that determines the fraction of the power generated by boundary-layer thermals (k_{th}) or wakes (k_{wk}) that is effectively used for convective lifting. It can also be increased by taking into account an additional contribution to the lifting, that might be stronger over ocean than over land. As done in closures based on CAPE or moisture convergence, we will consider a direct effect of the large-scale on convection, by adding the contribution of the large-scale convergence of mass below cloud base to the lifting.

The vertical velocity at the level of free convection has been fixed to 1 m s^{-1} (Rio et al. 2009; Grandpeix and Lafore 2010). However, observational studies have shown that the vertical velocity within convective updrafts is weaker over tropical ocean than over land in convective situations (Lemone and Zipser 1980; Zipser and Lemone 1980; Jorgensen and Lemone 1989; Lucas et al. 1994). This finding is also consistent with cloud resolving model simulations (Xu and Randall 2000). The slower vertical velocity at cloud base over ocean than over land is related to a lower lifting condensation level (LCL) in a more humid environment. By the time they reach their LCL, parcels undergo stronger acceleration when the LCL is higher. The inhibition, on the other hand, can either increase or decrease the mean vertical velocity of a population of updrafts between LCL and LFC. Indeed, the slowest parcels are stopped by the inhibition, while the fastest are slowed down, so that the mean can increase, decrease or not vary. Considering a population of updrafts of different strength and size however, the mean vertical velocity usually increases from cloud base to the upper part of clouds, as shown in observations by Lemone and Zipser (1980) and Zipser and Lemone (1980) for example, so that we will assume that the higher the LFC, the stronger the mean updraft vertical velocity at LFC. This choice is rather arbitrary, and we could have chosen to make w_b vary with PLCL rather than PLFC, the important point being to have a w_b varying among different environmental conditions. Figure 3 shows an estimation of the mean updraft vertical velocity at the level of free convection diagnosed from the DHARMA CRM simulation by applying a cloud sampling (only grid-cells with a liquid water content exceeding 10^{-6} kg kg^{-1} at LFC are considered, black crosses). Results show that the mean updraft vertical velocity at LFC varies from 0.4 m s^{-1} during the active period to 1 m s^{-1} during the suppressed period. A constant value for w_b is thus not adapted to various environmental conditions.

From those considerations, a set of sensitivity experiments is designed in order to be tested both on 1D case studies and full 3D simulations. As above, simulation WB1 corresponds to the original version of the ALP closure, for which $w_b = 1$ m s^{-1} and $\mathrm{ALP} = \mathrm{ALP}_{th} + \mathrm{ALP}_{wk}$, with $k_{th} = 0.5$ and $k_{wk} = 0.25$.

In experiment WB05, the vertical velocity at level of free convection is set to 0.5 m s^{-1}.

In experiment NP, w_b is no longer imposed as a fixed value but depends on the simulated level of free convection in the convective region via:

$$w_b = \frac{w_{b_{max}}}{1 + \Delta P/(p1 - plfc)} \tag{7}$$

where p1 is the pressure in the first model level and plfc the pressure at the level of free convection. Here $w_{b_{max}} = 6$ m s^{-1} and $\Delta P = 500$ hPa so that w_b varies slowly from values close to 0.5 for a LFC close to 950 hPa to values greater than 1 for a LFC exceeding 900 hPa. Although quite arbitrary, this formulation permits to capture the main evolution of w_b over the active and suppressed periods of TWP-ICE as shown in Fig. 3, even if it is still overestimated from 21st to 23rd of January.

In experiment ALPBLK, the conversion-efficiency parameter from boundary-layer thermals k_{th} is increased from 0.5 to 1. Sensitivity tests to k_{wk} were also performed but conclusions are quite the same as for k_{th} so that they are not shown here.

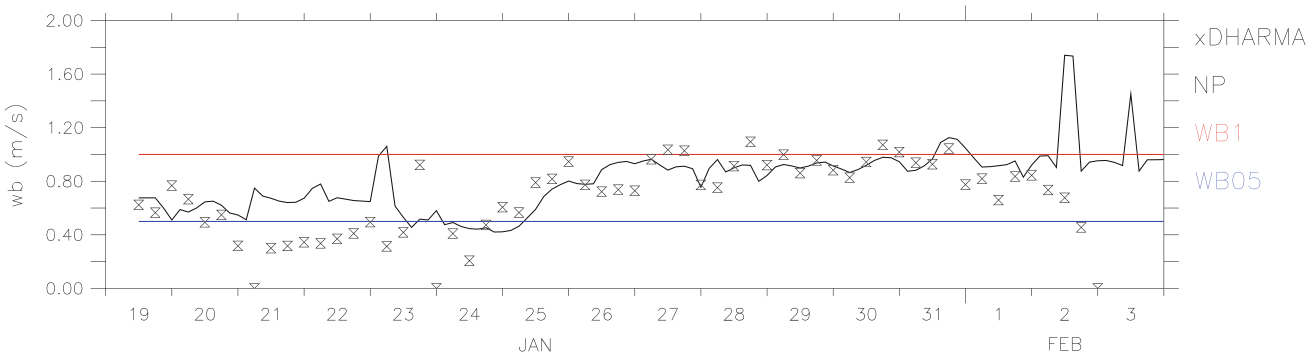

Fig. 3 Vertical velocity at level of free convection as simulated with the NP (*black*) and as imposed in WB1 (*red*) and WB05 (*blue*) versions of the LMDZ model in 1D mode. Results are compared with DHARMA (*black crosses*), for which w_b is computed using the "cloud" sampling

In experiment ALPCV, we consider the additional contribution to the lifting from large-scale convergence below the cloud base. The available lifting power is thus computed from $ALP = ALP_{th} + ALP_{wk} + ALP_{cv}$, with $ALP_{cv} = -k_{cv}MIN(\omega_{950hPa},0)$. Parameter k_{cv} is arbitrarily tuned to 0.2, in order to obtain a significant increase of deep convection intensity in 1D and 3D simulations.

The various experiments are summarized in Table 1 which describes the closure type as well as the values of parameters involved in the ALP closure.

2.4 Impact on simulated precipitation

The partitioning between convective and large-scale precipitation for all sensitivity experiments is shown in Fig. 2 for the TWP-ICE case study. All sensitivity tests yield a re-intensification of convective precipitation during the active period. The weakest effect is obtained from increasing the conversion efficiency parameter from the boundary-layer thermals (ALPBLK, lightblue). Decreasing w_b during the active period (WB05, blue and NP, black) or increasing the lifting power by convergence (ALPCV, green) both intensify deep convection, even if it is not sufficient to generate as much convective precipitation as in observations during the night from 23 to 24 January, the strongest event of TWP-ICE. Averaged over the active period, convective precipitation represents 50 % of total precipitation in ALPCV, 60 % in WB05 and 57 % in NP. In all simulations as in observations, precipitation is almost only convective during the suppressed period.

The effect of the various sensitivity experiments on the representation of the diurnal cycle of continental convection is illustrated in Fig. 1. Adding the contribution of low-level convergence (ALPCV, green) has no impact on that day as it is very weak. Increasing k_{th} (ALPBLK, light-blue) leads to an earlier onset and less precipitation but those effects remain weak. Decreasing w_b to 0.5 m s^{-1} clearly leads to a premature maximum and extinction of precipitation. In simulation NP (black line), in which w_b value is a little more than 1 m s^{-1}, precipitation increase is more gradual than in WB1 leading to values closer to the MESO-NH simulation.

From those results, two simulations reconcile mid-latitude continental convection and tropical oceanic convection, namely simulations NP and ALPCV. In the first one, convection is controlled only by sub-grid processes with a vertical velocity at LFC varying according to environmental conditions. In the second one, the vertical velocity at LFC is kept constant and a contribution from the large-scale is added to the lifting power, so that convection is controlled both by sub-grid processes and large-scale convergence. The NP version based solely on sub-grid processes to the lifting is the version that was retained for the climate simulations performed for CMIP5 (Hourdin et al. 2012, this issue). In the following, we will extend our evaluation and analysis to the representation of mean environmental properties and sub-cloud lifting processes. For this, we will focus on the version of the model presented in Hourdin et al. (2006) (SP), the version of the model with the original ALP closure (WB1), and the version of the model with the revisited ALP closure (NP). The concept of introducing an additional large-scale contribution to the lifting like in ALPCV will also be discussed further.

Table 1 Sensitivity experiments to closure type and parameters involved in the ALP closure

Simulation	Closure type	k_{th}	k_{cv}	w_b
SP	CAPE	–	–	–
WB1	ALP	0.5	0	1
WB05	ALP	0.5	0	0.5
NP	ALP	0.5	0	Eq. 7
ALPBLK	ALP	1	0	1
ALPCV	ALP + convergence	0.5	−0.2	1

3 Convection over tropical ocean

3.1 Impact of convection on the large-scale

Figure 4 shows the vertical profiles of potential temperature and specific humidity, averaged over either the active (up to 300 hPa, upper panel) or the suppressed (up to 750hPa, lower panel) period of TWP-ICE for simulations DHARMA, SP, WB1 and NP. Simulation WB1 is too warm (except between 850 and 550 hPa during the suppressed period) and too moist over both periods. As deep convection is too weak in this simulation, the near surface layer gradually warms and moistens, leading to a drop in surface fluxes and no convection at all from January the 23rd to the 29th, until boundary-layer turbulence recovers and initiates new convection (not shown). By contrast, simulation SP is too cold and dry, while simulation NP gives results the closest to DHARMA. During the suppressed period, the boundary layer is homogeneous in NP while more stable in DHARMA. This could be related to an overestimation of the activity of thermals in comparison with the activity of wakes in the NP simulation.

The evolution of CIN, CAPE, PLCL (pressure at the lifting condensation level) and PLFC (pressure at the level of free convection) computed from mean large-scale variables are displayed in Fig. 5 for the same simulations. The absence of deep convection in simulation WB1 is

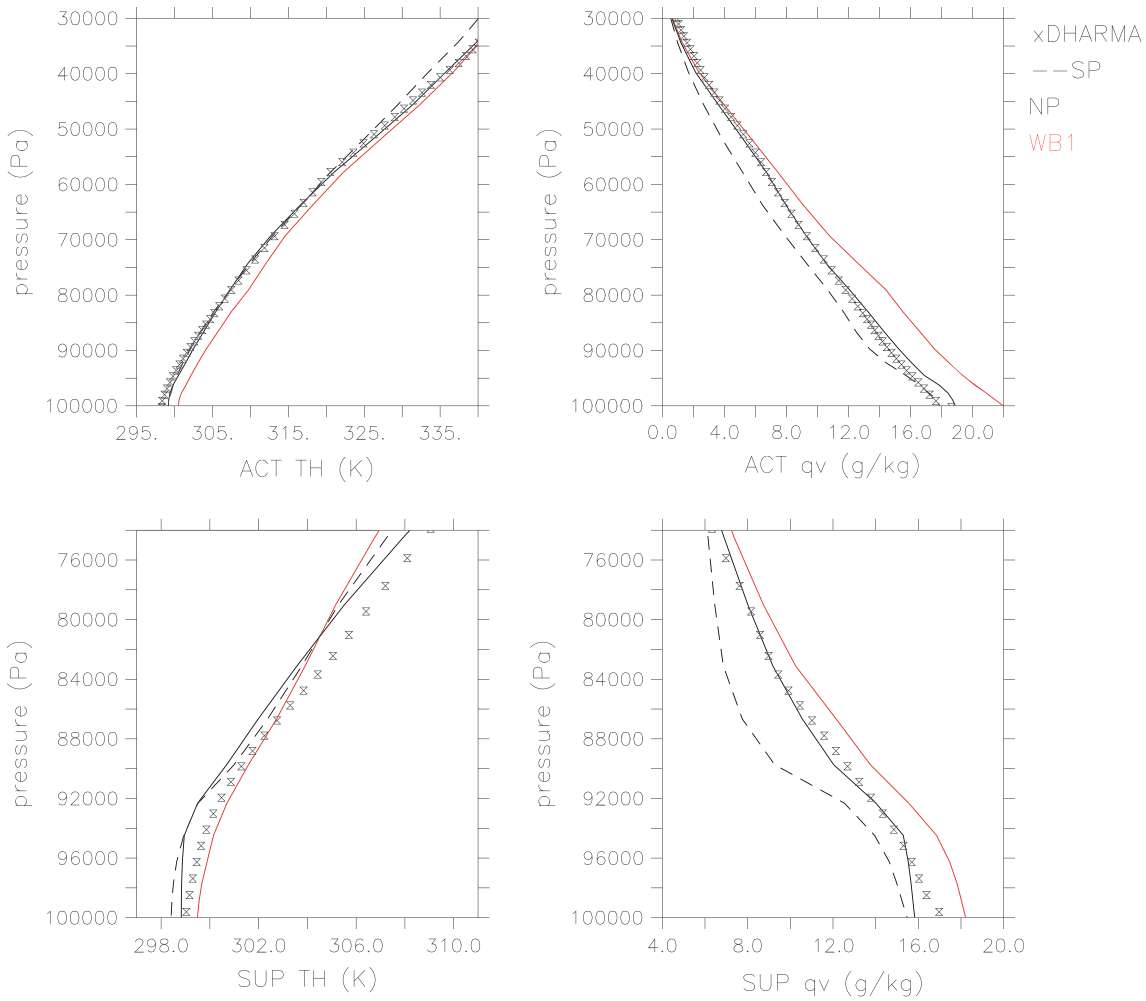

Fig. 4 Vertical profiles of potential temperature (*left*, K) and specific humidity (*right*, g kg^{-1}) averaged over the active (*top*) and suppressed (*bottom*) periods of the TWP-ICE case as simulated with different versions of the LMDZ model in 1D mode: SP (*black dash*), NP (*black*), WB1 (*red*). Results are compared with DHARMA CRM (*black crosses*)

associated with a strong overestimation of the CAPE. Despite a better representation of the vertical profiles averaged over both periods, simulation NP underestimates the CIN and overestimates the CAPE during the active period. In particular, the CIN fluctuates much more. Note that the CAPE is overestimated in both NP and SP during the two strongest events (January 19th and 23rd) of the active period, suggesting that neither the CAPE nor the ALP closure can reproduce the particular strength of those events. However, the simulation of those strong convective events could also be an issue for DHARMA, as the size of the domain and the boundary cyclic conditions may lead to some mis-representation of the systems in their development and dissipation stages. This is particularly true for the 23rd, for which the convective system was particularly large. This question is being investigated further by Zhu et al. (2012) comparing CRMs with limited area models. The condensation level is well-captured in SP and NP, while the level of free convection tends to be underestimated during the active period, in consistency with the underestimation of the CIN. While PLCL is lower during the active than the suppressed period, there is no such evidence for PLFC when considering the whole domain averaged environmental properties. However, in the new set of parameterizations, convective towers do not form in the mean environment but outside the cold pool region, so that their environment is much more unstable than the mean environment over the total domain including stable cold pools. This is discussed further in the next section.

3.2 Convective versus cold pool region

As soon as a wake is active, the grid cell is decomposed into the wake and the off-wake regions. The evaporation of precipitation takes place within the wake region, while the convective updrafts form in the environment of the wakes. In

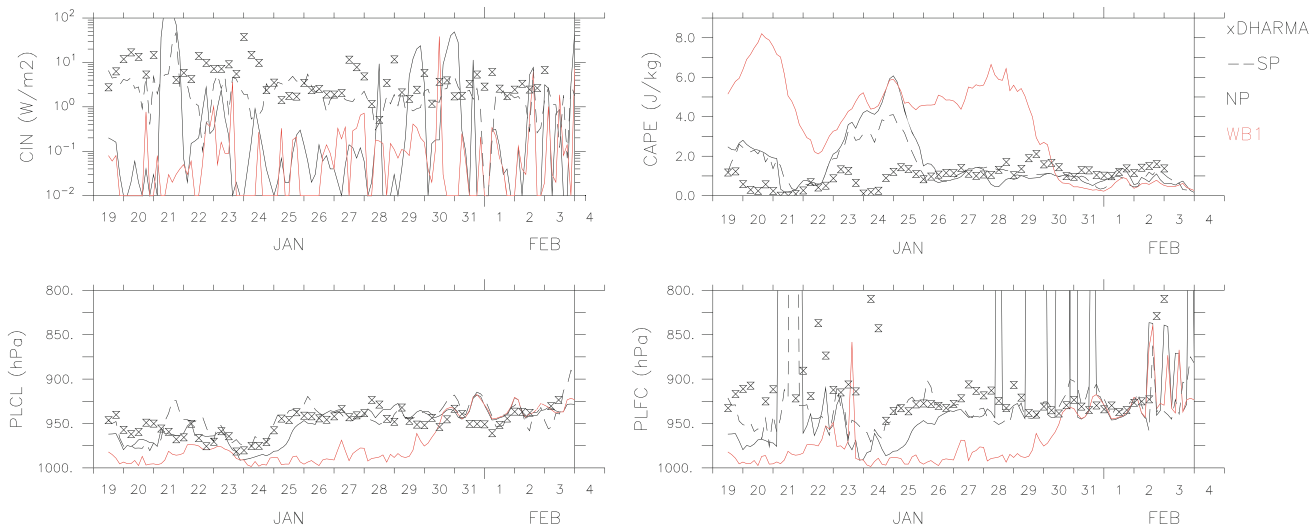

Fig. 5 Time evolution of the convective inhibition (CIN, J kg^{-1}), the convective available potential energy (CAPE, kJ kg^{-1}), the condensation level (PLCL, hPa) and the level of free convection (PLFC, hPa) during the TWP-ICE case as simulated with different versions of the LMDZ model in 1D mode: SP (*black dash*), NP (*black*), WB1 (*red*) and with DHARMA CRM (*black crosses*). Variables are computed from lifting a parcel from the 150 m level

particular, CIN, CAPE, PLCL and PLFC seen by the deep convection scheme are computed using the virtual potential temperature averaged over the environment of wakes, so that the ascending parcel has different properties from that of a parcel with mean environmental properties as used to compute variables displayed in Fig. 5. The sub-grid variability of CIN, CAPE, PLCL and PLFC in simulation NP is illustrated in Fig. 6. In the off-wake region (ENV), the convective inhibition is close to zero most of the time, so that PLCL and PLFC coincide, PLFC being lower during the active than during the suppressed period, as expected. The CIN in the wake region (WK) is quite close to the mean inhibition simulated by DHARMA (Fig. 5), which suggests that fluctuations of the mean inhibition in NP seen in Fig. 5 could be due to an overestimation of the fraction of the grid-cell attributed to the environment of wakes in comparison with the wake region. The sub-grid variability of CAPE is low in relation with a higher relative humidity in the wake region. The stronger w_b during the suppressed than the active period is not associated with a higher or lower CIN, and is probably due to a more active and deep boundary-layer yielding stronger updrafts. Those results illustrate the importance of partitioning the model grid-cell into the convective and the wake regions, as the environment in which convection occurs is quite different from the mean environment over the total grid cell including wakes.

3.3 Third-order moment of vertical velocity at the condensation level

The available lifting power is a measure of the third order moment of vertical velocity at cloud base. The third-order moment of vertical velocity resolved by DHARMA at the condensation level is shown in Fig. 7 (black crosses). Surprisingly, we note that $\overline{w'^3}$ is smaller during the active period than during the suppressed period. This point is related to the deeper boundary-layer during the suppressed period (higher LCL) and drier conditions that favor rain evaporation and cold pools development. Note that the horizontal resolution of DHARMA is 900 m here, so that the potential contribution of smaller scales to $\overline{w'^3}$ would not be seen. In simulations WB1 and NP, $\overline{w'^3}$ can be estimated by:

$$\overline{w'^3} = \frac{2ALP_{th}}{\rho k_{th}} + \frac{2ALP_{wk}}{\rho k_{wk}} \tag{8}$$

also shown in Fig. 7. As already discussed, surface fluxes are very weak in simulation WB1 until the end of January so that turbulence and convection vanish and $\overline{w'^3}$ is zero. Simulation NP is able to reproduce the increase of $\overline{w'^3}$ on the strongest events of the active period and its larger values during the suppressed period. However it is overestimated during the active period and the end of the suppressed period, in relation with either excessive wake or thermal contributions.

3.4 Sub-grid versus large-scale closures

Finally, the resulting mass flux at LFC is evaluated by comparison with the mass-flux resolved in DHARMA applying the cloud sampling (top panel of Fig. 8). A notable feature is that the mass flux in DHARMA is of the same order of magnitude during the active and the

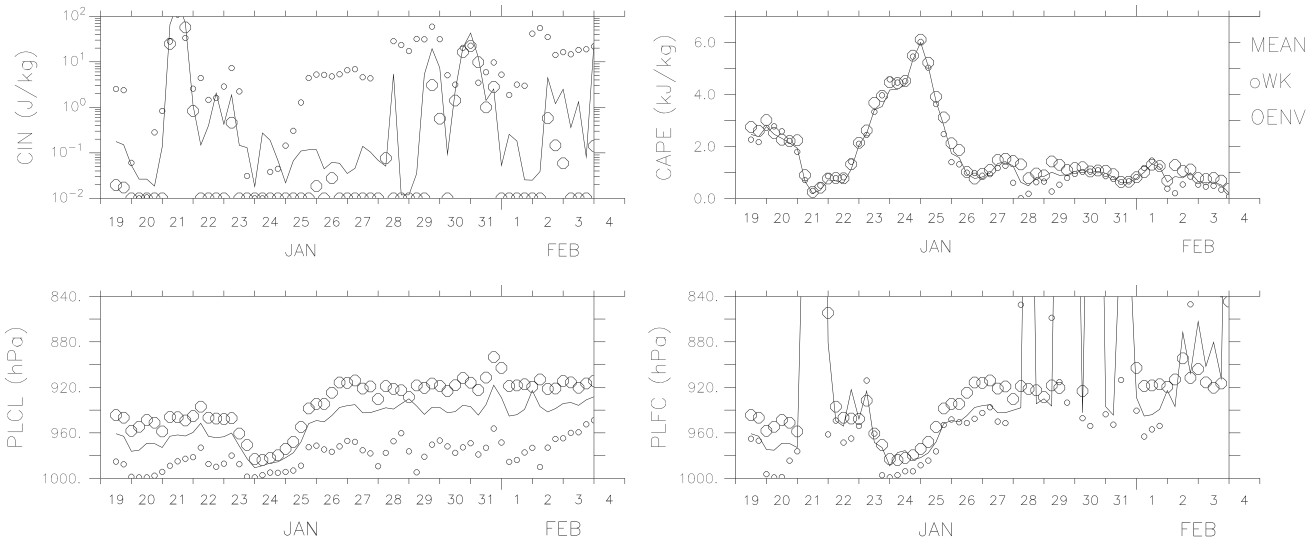

Fig. 6 Time evolution of the convective inhibition (CIN, J kg^{-1}), the convective available potential energy (CAPE, kJ kg^{-1}), the condensation level (PLCL, hPa) and the level of free convection (PLFC, hPa) averaged over the total grid cell (full line, as in Fig. 5), over the cold pool region (*small circles*) and over the environment of wakes (*large circles*) as simulated in NP during TWP-ICE

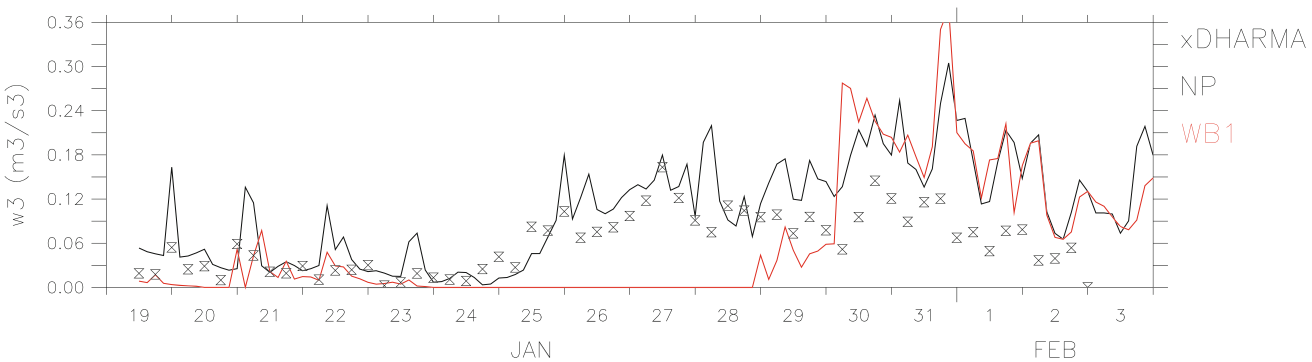

Fig. 7 Third-order moment of vertical velocity at condensation level as simulated with the NP (*black*) and WB1 (*red*) versions of the LMDZ model in 1D mode and as resolved by DHARMA CRM (*black crosses*)

suppressed periods, suggesting that the intensity of deep convective events does not only rely on the mass flux available at the cloud base. Lateral entrainment and detrainment, as well as formation of a meso-scale organization may also contribute to the deep convection intensity. Note that the cloud sampling does not allow to distinguish shallow from deep convective clouds so that this mass flux includes the contribution of small shallow clouds, congestus clouds and deep convective towers. The mass flux computed from the CAPE closure in simulation SP, which aims to represent both shallow and deep convective clouds, is underestimated during the whole active period in comparison to DHARMA, particularly for the 19th and 23rd of January. It is more consistent with the CRM during the suppressed period. In simulation NP, as CIN is close to zero, the mass flux is relatively in phase with the lifting power. However, w_b is close to 0.5 m s^{-1} during the active period and close to 1 m s^{-1} during the suppressed period, so the mass flux is actually of the same order of magnitude over the whole period. As shallow clouds are represented via the thermal plume model in NP, the cloud-base mass flux from the deep convection scheme shown in the top panel of Fig. 8 underestimates the total mass flux when compared to DHARMA. The contribution from thermals is added to the mass flux from deep convection in the bottom panel of Fig. 8. Results are then more consistent with DHARMA even if the contribution from boundary-layer thermals appear to be overly strong on some days, as on the 22th of January or during the end of the suppressed period. This is consistent with an overestimated $\overline{w'^3}$ on those days and suggests that the thermal plume model is overly active. In contrary with the deep convection scheme, the thermal plume model is active in the mean environment and not only in the environment of wakes. Partitioning the thermal plume model contribution in the wake and off-wake regions would probably modify thermal behavior and work

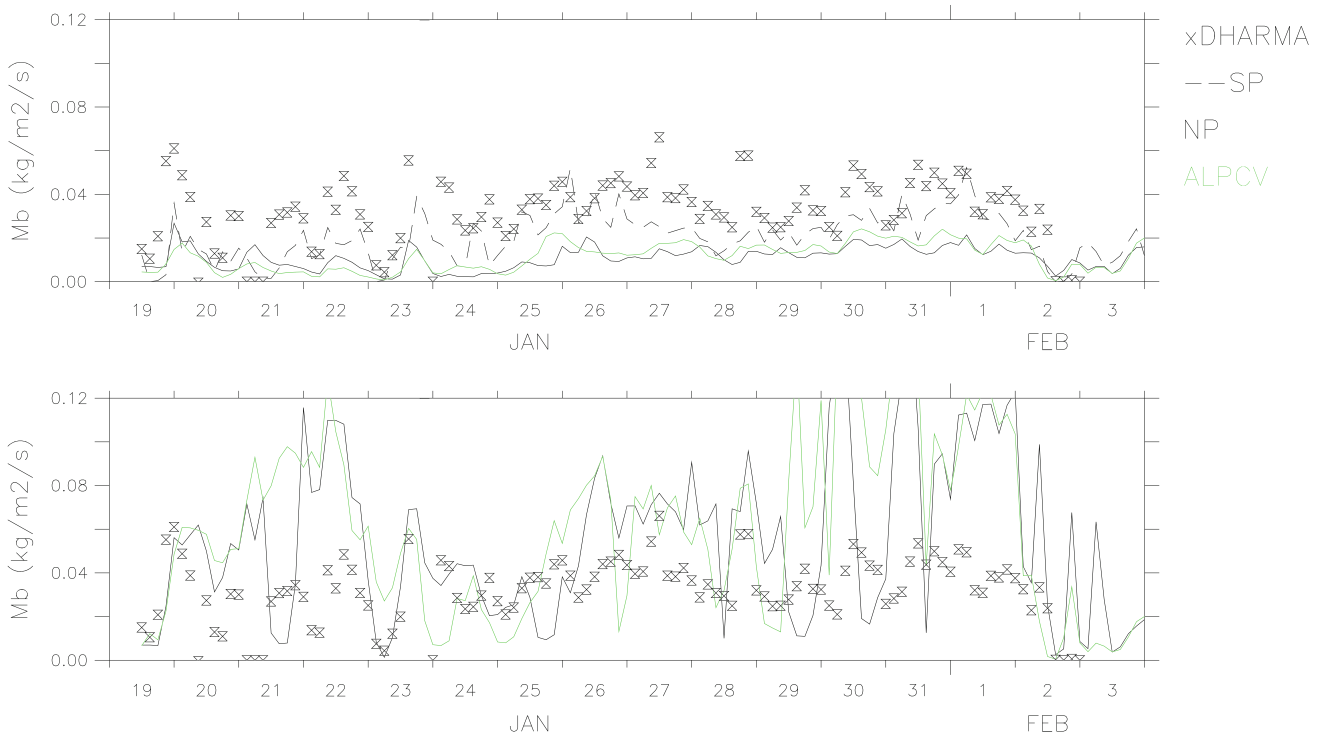

Fig. 8 Time evolution of the cloud-base mass flux during TWP-ICE as simulated with different versions of the LMDZ model in 1D mode: SP (*black dash*), NP (*black*) and ALPCV (*green*), and with DHARMA CRM (*black crosses*). The bottom panel shows the total contribution from thermals and deep convection to the mass flux at LFC in simulation NP and ALPCV compared to DHARMA. In DHARMA, M_b is computed using the "cloud" sampling, i.e. retaining only the *grid* cells in which the condensed water exceeds 10^{-6} kg kg^{-1}

is in progress in that direction. For information, the mass flux at LFC simulated by simulation ALPCV is also shown in Fig. 8. The increase of the lifting power by the large-scale convergence in ALPCV has an equivalent impact than the decrease of w_b in NP on that case, and results are quite similar between the two simulations.

To evaluate further the relevance of relating the cloud-base mass flux to either the CAPE, $\overline{w'^3}$ at LCL or low-level convergence, we explore the relationship between the mass flux at LFC and those different quantities in the CRM. Results are shown in Fig. 9 separately for the active (top) and suppressed (bottom) periods. No significant link is found between the mass flux and the CAPE either during the active or the suppressed period (left panel). A stronger link is found between the mass flux and $\overline{w'^3}$ at LCL, particularly during the active period but also during the suppressed one (middle panel). The ratio of M_b over $\overline{w'^3}$ is larger during the active than the suppressed period, which is consistent with a lower CIN and w_b during the active period when considering Eq. 2. A link also exists between the mass flux and the low-level convergence during the active period, but not during the suppressed period. However, it is impossible to infer what is a cause or a consequence of deep convection. As also highlighted by Kuang and Bretherton (2006) when evaluating the closure based on CIN and the boundary-layer turbulent kinetic energy proposed by Bretherton et al. (2004), those results favor closures based on sub-cloud processes rather than on CAPE in oceanic conditions.

4 Diurnal cycle of convection over semi-arid land: The AMMA case study

The WB1 version of the new set of parameterizations was extensively evaluated on the continental EUROCS case by Rio et al. (2009). As already shown, simulations ALPBLK, ALPCV, WB1 and NP give similar results on this case while the WB05 version fails in shifting convection to late afternoon (Fig. 1). Here we rather focus on a continental case study in a semi-arid environment over the Sahel, for which the various versions of the ALP closure show more contrasted behavior.

4.1 Diurnal cycle of convection on the AMMA case study

This case study (Couvreux et al. 2012) was built from observations (Lothon et al. 2011) collected in Niamey on 10 July 2006 in the framework of the African Monsoon

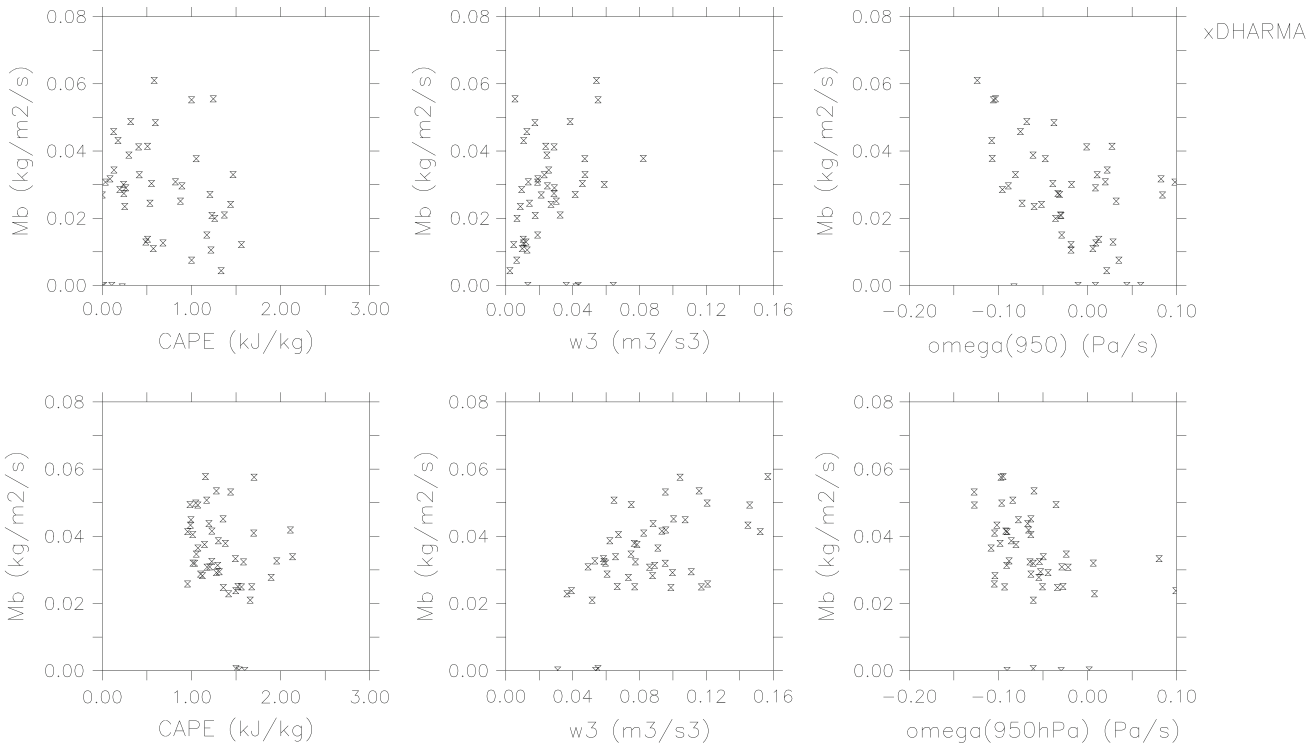

Fig. 9 Scatter plots of the mass flux at level of free convection (M_b, kg m^{-2} s^{-1}) and the convective available potential energy (CAPE, kJ kg^{-1}) (*left*), the third-order moment of vertical velocity at LCL ($\overline{w'^3}$, m^3 s^{-3}) (middle) and the convergence at 950 hPa (Pa s^{-1}, right) for the active (*top*) and suppressed (*bottom*) periods of TWP-ICE as simulated by the DHARMA CRM

Multidisciplinary Analysis (AMMA) experiment. Semi-arid conditions observed in Niamey are quite distinct from the mid-latitudes conditions of the EUROCS case. Latent heat flux is low (30 vs. 400 W m^{-2} for the EUROCS case) and sensible heat flux is high (300 vs. 120 W m^{-2}) leading to a Bowen ratio of 10 (vs. 0.3). In addition, the convective boundary layer is thicker (3 km instead of less than 2 km) and, while it is in phase with the insolation in the EUROCS case, the observed convective available potential energy decreases during the day (Couvreux et al. 2012), which is challenging for convection schemes with a CAPE closure. The convective system observed that day was relatively small, and only 2 stations reported precipitation, one giving 7 mm at 18:00UTC and the other 18 mm between 17:00UTC and 20:00UTC. Surface fluxes and radiative tendencies are prescribed, so that the surface and radiation schemes are switched off. High resolution simulations of the case have been performed with MESO-NH (Couvreux et al. 2012). Here we rely on a simulation run from 6:00LT to 18:00LT over a domain of 100 × 100 km with a horizontal resolution of 200 m, a time-step of 2 s, and cyclic lateral boundary conditions.

The diurnal cycle of the simulated precipitation is displayed in Fig. 10 for the various sensitivity experiments presented in Sect. 2.3. In MESO-NH as in observations, the transition from shallow to deep convection occurs quite

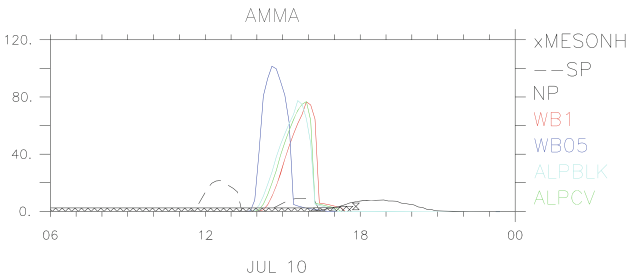

Fig. 10 Diurnal cycle of precipitation in AMMA case simulated with different versions of the LMDZ model in 1D mode: SP (*black dash*), NP (*black*), WB1 (*red*), WB05 (*blue*), ALPBLK (*light blue*), ALPCV (*green*) and compared with results from MESO-NH (*black crosses*)

late, later than during the EUROCS case. Precipitation starts around 16:00LT and increases slowly until 18:00LT where the LES simulation stops because the domain size is too small to correctly simulate later deep convection development. A similar behavior is seen in this case as for the EUROCS case for simulations SP, WB1, WB05 and ALPBLK. Precipitation peaks to early at midday in SP, while the maximum is shifted to 16:00LT in WB1. Increasing the available power provided by thermals has a weak impact and leads to slightly earlier precipitation, as does the low-level convergence (ALPCV). Decreasing w_b to 0.5 m s^{-1} makes the onset of precipitation and the maximum occur even earlier. In this case, only the NP

simulation, in which w_b depends on the level of free convection (and is of the order of 1.75 m s^{-1} at initiation time), permits a delay in the increase of convection intensity. In this case, precipitation becomes significant around 15:00LT and the maximum occurs around 18:00LT, in better correspondence with the reported observations. It is noteworthy that it is not the trigger of the convection scheme which is delayed between WB1 and NP, but the gradual increase of convection intensity which is slower and delays precipitation, in relation with a higher vertical velocity at the level of free convection which increases the lifting power lost by dissipation.

As was done for the oceanic case, we now focus the discussion on the comparison between the LMDZ physical package with CAPE closure (SP), the original version of the ALP closure (WB1) and the new ALP closure (NP). Note that the version with a large-scale contribution to the lifting, ALPCV, is not able to capture the late precipitation observed in that case.

4.2 Impact of convection on large-scale profiles

Figure 11 shows the vertical profiles of potential temperature and specific humidity, simulated around initiation time at 16:00LT (top) and after deep convection initiation at 18:00LT (bottom) for simulations MESO-NH, SP, WB1 and NP. The better representation of potential temperature profile at 16:00LT in WB1 and NP compared to SP comes from the representation of the non-local transport within the boundary layer by thermals, accounted for by the thermal plume model (Rio and Hourdin 2008). At 16:00LT, in simulation WB1, the mid-troposphere is too warm and dry, while the lower levels are too cold and moist, as a result of premature deep convection development (as illustrated by precipitation in Fig. 10). This is even more pronounced in simulation SP. Vertical profiles simulated with NP are close to MESO-NH results at deep convection initiation time. At 18:00LT, simulation NP is the closest to MESO-NH, even if convection tends to moisten and cool low-level too rapidly in comparison with MESO-NH. This is probably related to a still too early onset of convection and precipitation in simulation NP compared with MESO-NH.

The corresponding CIN, CAPE, PLCL and PLFC are displayed in Fig. 12. Note that simulations WB1 and NP are identical until deep convection initiation time. The CIN drops to zero around 11:00LT in SP and around 12:00LT in WB1 and NP, which is not the case in MESO-NH simulation even if the simulated CIN is low and less than 1 J kg^{-1}. The growth of convective inhibition after

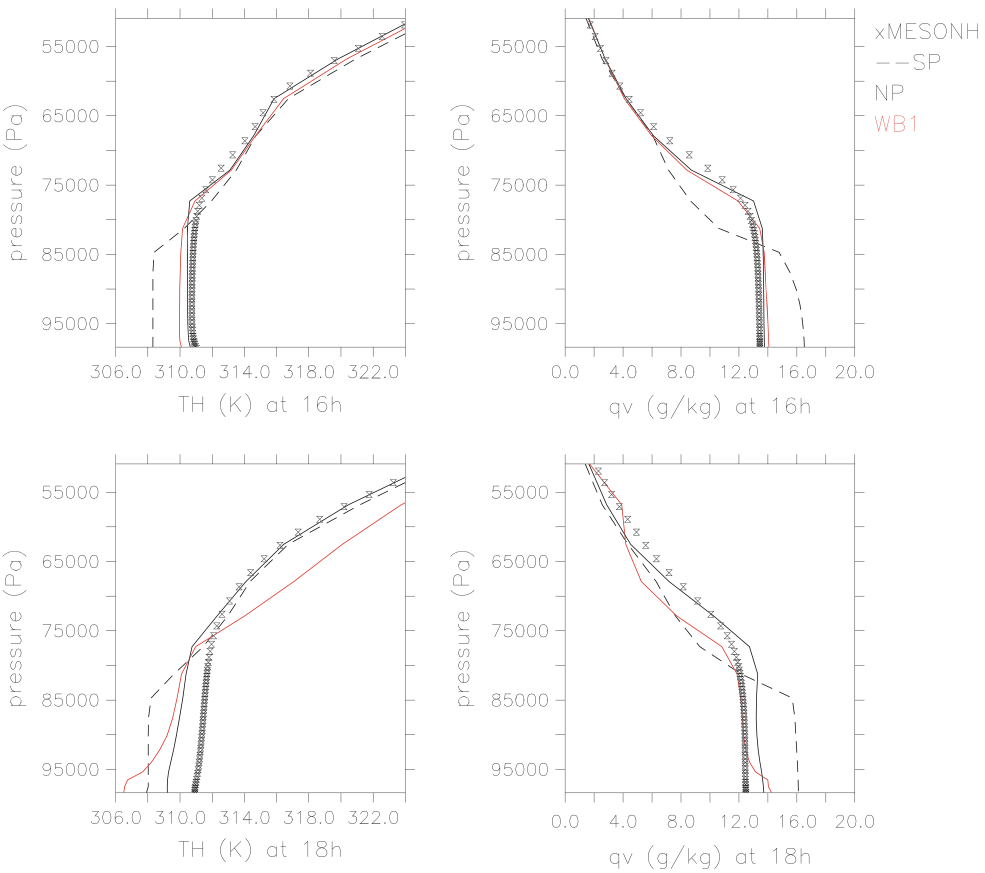

Fig. 11 Vertical profiles of potential temperature (*left*, K) and specific humidity (*right*, g kg^{-1}) at 16:00LT (*top*) and 18:00LT (*bottom*) in the AMMA case as simulated with different versions of the LMDZ model in 1D mode: SP (*black dash*), NP (*black*), WB1 (*red*) and with MESO-NH (*black crosses*)

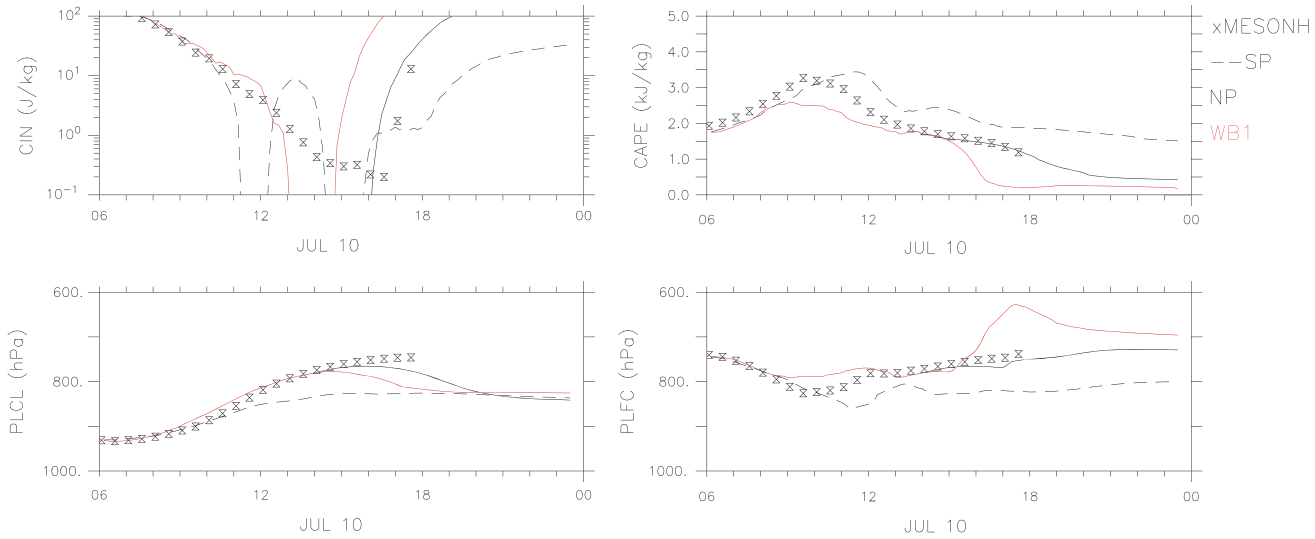

Fig. 12 Diurnal cycle of the convective inhibition (CIN, J kg^{-1}), the convective available potential energy (CAPE, kJ kg^{-1}), the condensation level (PLCL, hPa) and the level of free convection (PLFC, hPa) during the AMMA case as simulated with different versions of the LMDZ model in 1D mode: SP (*black dash*), NP (*black*), WB1 (*red*) and with MESO-NH (*black crosses*). Variables are computed from lifting a parcel from the 150 m level

16:00LT in MESO-NH is well-reproduced by simulation NP even though earlier. In MESO-NH, the CAPE evolution results from the strong daytime boundary layer growth within a dry free troposphere and CAPE decreases because the low level specific humidity sharply drops (See Couvreux et al. 2012). CAPE is maximum at 9:30LT and decreases afterward while deep convection starts at 16:00LT. The non-correlation between CAPE and convection intensity is thus clear on that case. Indeed, the CAPE is overestimated in simulation SP, with a maximum at 11:00LT instead of 9:30LT in MESO-NH. The diurnal evolution of CAPE, PLCL and PLFC is better captured in simulations WB1 and NP. The abrupt decrease of CAPE and increase of level of free convection at 16:00LT in simulation WB1 is related to an overly intense convection at 15:00LT.

4.3 Precipitation timing and sub-grid variability of CIN

As cold pools start to form in late-afternoon, the sub-grid partitioning between the wake region and its environment is only effective after that time. It is still an important component of the new set of parameterizations as this partitioning plays a role in the duration of the event. In simulation NP, deep convection is active as long as the available lifting energy provided either by thermals or

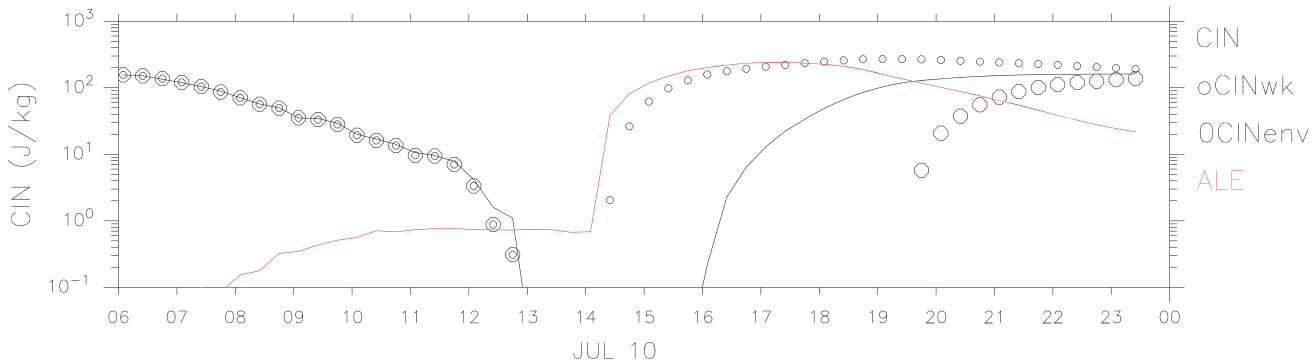

Fig. 13 Sub-grid variability of the convective inhibition (CIN, J kg^{-1}) in the AMMA case as simulated with the NP version of LMDZ. The mean CIN over the total domain (*black line*) is decomposed into the CIN in the wake region (*small circles*) and the CIN in the environment of wakes (*large circles*). The CIN seen by the convection scheme (environment of wakes, *large circles*) has to be compared to the available lifting energy (ALE, J kg^{-1}) (*red line*) to determine deep convection timing

wakes overcomes the convective inhibition. The sub-grid variability of the CIN is displayed in Fig. 13 for simulation NP. The inhibition increases rapidly in the wake region as soon as wakes are active, whereas it remains lower in the environment of wakes. As a result, the CIN seen by the convection scheme increases three hours later than the mean inhibition. The available lifting energy is also shown in Fig. 13. The CIN becomes smaller than the available lifting energy around 13:00LT and deep convection is triggered. However deep convection stays weak until 16:00LT in relation with the closure specification. This suggests that the triggering still occurs too early in simulation NP, but this is weakened by the closure specification that yields weak convection until 16:00LT. Deep convection is active until the convective inhibition increases and overcomes ALE again. Considering CIN in the environment of wakes instead of in the mean grid-cell allows the maintenance of deep convection for a longer period of time, until 21:00LT instead of 19:00LT.

4.4 Parameterization of the third order moment of vertical velocity

As the MESO-NH simulation stops after deep convection initiation, we focus here on the third order moment of vertical velocity generated by thermal plumes before deep convection initiation. To extract thermal plume contribution to $\overline{w'^3}$ in the LES simulation, a simulation is performed in which a tracer with a life time of 15 min is emitted at the surface with a constant flux. A conditional sampling based on the tracer concentration is then applied to select ascending plumes from the surface to their top as done in Couvreux et al. (2010). Once thermals are characterized, their mean vertical velocity and fractional coverage can be deduced and used to compute the corresponding $\overline{w'^3}$ via Eq. 4. The result is shown in the left panel of Fig. 14. The sampling characterizes the ascending updrafts so that deep convective towers not represented by the thermal plume model in the SCM after 16:00LT are also sampled in the LES. The diurnal cycle of the vertical profile of $\overline{w'^3}$ given by the thermal plume model (Eq. 4) is shown in the right panel of Fig. 14. Before convection initiation, the evolution of the vertical profile of the parameterized $\overline{w'^3}$ is qualitatively comparable with MESO-NH. The parameterized $\overline{w'^3}$ increases too rapidly with a maximum at 13:00LT instead of 14:00LT. Thermals also vanish too rapidly in simulation NP after 16:00LT, probably due to the activation of the deep convection and cold pool schemes which tend to stabilize low levels and inhibit thermal plumes prematurely. Also, the order of magnitude of $\overline{w'^3}$ is approximately three times lower in NP than in MESO-NH. Indeed, the thermal plume model has never been evaluated in such semi-arid conditions where the boundary-layer is such deep and apparently underestimates thermal buoyancy and velocity. The shortcomings of the thermal plume model in such environment will be investigated further in the future. In the present simulation, the underestimation of $\overline{w'^3}$ is however maximum in the middle of the boundary-layer and smaller near the cloud base, and the underestimation of $\overline{w'^3}$ provided by thermals may be compensated by the value of parameter k_{th}.

It is noteworthy that while the thermals activity was overly strong over ocean in the TWP-ICE case-study, it is too weak here in semi-arid conditions. This highlights the difficulty to develop a parameterization valid for all environments encountered over the globe. Even if the representation of sub-grid sub-cloud processes needs to be improved further, the version of the model with the new ALP closure formulation significantly improves the timing of convection over land, while simulating satisfactorily the convection intensity over ocean. The last section explores if those behaviors are reproduced in the 3D version of the model.

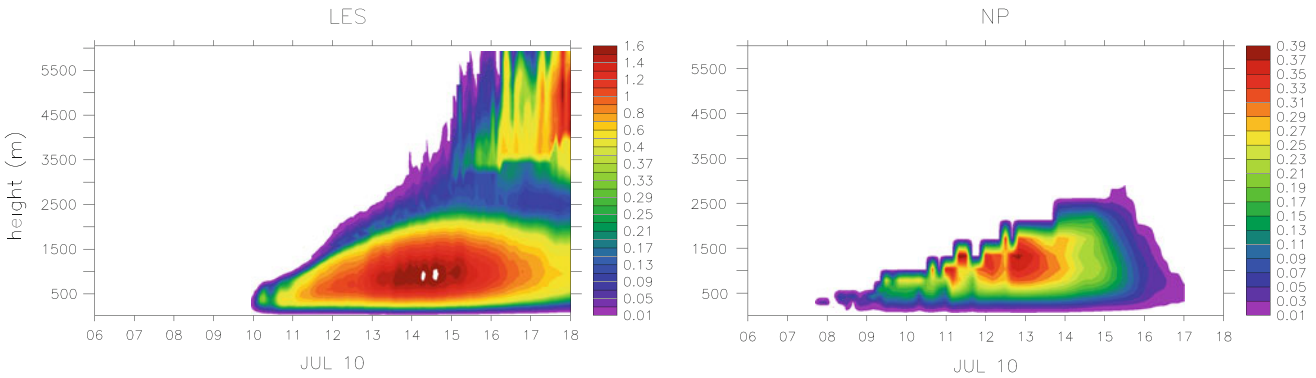

Fig. 14 Third order moment of vertical velocity ($m^3\ s^{-3}$) as simulated by MESO-NH within thermals (*left*) and as parameterized by the thermal plume model in simulation NP (*right*). Thermals are identified in the LES simulation using a tracer-based sampling. Note that the two *colorbars* are different

5 Global simulations

Finally, 10-year imposed-SST sensitivity experiments with the full 3D LMDZ5 model are presented. The horizontal grid is based on 96 by 95 points regularly spread in longitude and latitude and a 39-level vertical grid and 7′30″ time-step are used. All simulations with the ALP closure are run with the same values of the model tunable parameters. Note that parameter tuning was shown to be less important for precipitation mean and variability than the physical parameterizations used (Hourdin et al. 2012, this issue). In the following, simulations are compared with precipitation observation from Global Precipitation Climatology Project Dataset (GPCP, Huffman et al. 2001) and from the Tropical Rainfall Measuring Mission (TRMM, Kummerov et al. 2001).

5.1 Intensity of tropical convection

The global annual mean of precipitation for simulations SP and NP is already shown in Hourdin et al. (2012), this issue. Here we rather focus on the north hemisphere summer season, to highlight the monsoon season over land. The global mean precipitation from June to September is shown in Fig. 15 for observations and simulations SP, WB1, ALPCV and NP. Simulation SP tends to overestimate precipitation along the equator, which is amplified over ocean in simulation WB1. In simulation ALPCV, precipitation is amplified on the western part of the Pacific ocean and along the ITCZ, with some similarity with the behavior of the LMDZ3 version of LMDZ including the Tiedtke (1989) deep convection scheme based on a moisture convergence closure (Hourdin et al. 2006). It is noteworthy that the simulated mean precipitation is quite similar in all runs and not as much sensitive to the parameterizations used.

A dynamical regime framework, based on ω_{500} as in Bony et al. (2004), is used to illustrate the relationship between the large-scale dynamics and precipitation over tropical ocean (Fig. 16). The contribution from convective and large-scale precipitation are also shown in the middle and bottom panels. Interestingly, conclusions drawn in 1D regarding the partitioning between convective and non-convective precipitation hold on in 3D: more than half of the total precipitation is handled by the large-scale scheme in WB1, whereas precipitation is mostly convective in all the other simulations.

5.2 Diurnal cycle

The impact of the new set of parameterizations on the simulation of the diurnal cycle of convection in the 3D simulations is now investigated. Figure 17 displays the local hour of the first harmonic of the diurnal cycle of rainfall as observed by TRMM (3h data) and as simulated by SP, WB1, ALPCV and NP simulations (left panel) as a proxy for the local hour of maximum rainfall. Again, the same behavior as in the 1D case studies is obtained. On average, the maximum is around 12:00LT over land in SP, while it is delayed to 15:00LT in WB1. Simulation ALPCV yields earlier maximum than simulation WB1 in regions where low-level convergence is significant over land. The maximum rainfall is estimated around 17:00LT in simulation NP, in better agreement with TRMM observations, even though apparently still too early in that figure. The diurnal cycle of precipitation simulated with SP and NP is directly compared with TRMM observations on 5 specific regions in the right panel of Fig. 17. Over land, SP systematically simulates the maximum rainfall at midday, while NP simulates it around 18:00LT, as in observations. The shift in the local hour of the first harmonic of the diurnal cycle of rainfall previously mentioned is due to the fact that precipitation stops after 22:00LT in NP, while it slowly decreases through the night in observations. Over ocean, the difference between SP and NP is less, but simulation NP better captures the relatively steady character of precipitation.

The shift of continental precipitation to late afternoon obtained in the 1D version of the model by Rio et al. (2009) is thus confirmed here in the full 3D simulations, correcting a long-standing bias common to most GCMs.

5.3 Intraseasonal variability of precipitation

Finally, the intra-seasonal variability of precipitation is shown in Fig. 18 for JJAS and compared with observations. The difference of variability is impressive between the version with CAPE closure (SP) and all the versions with ALP closure. Simulation SP strongly underestimates precipitation variability, while it is overestimated in all other simulations. In simulation WB1, the underestimation of convection probably yields more large-scale precipitation that builds up more slowly than convective precipitation. Simulation ALPCV reduces this variability but it stays high in the West Pacific and too low over land. On the contrary, simulation NP significantly reduces the variability over ocean in comparison with WB1 while increasing it over land, in much better agreement with observations, even if the variability is still underestimated in regions of low variability (East Pacific and East Atlantic). The representation of convective processes at the local and daily scales thus seems to impact the variability of global precipitation at longer timescales.

6 Conclusions

A new concept based on the control of deep convection by sub-cloud lifting processes has been introduced in the

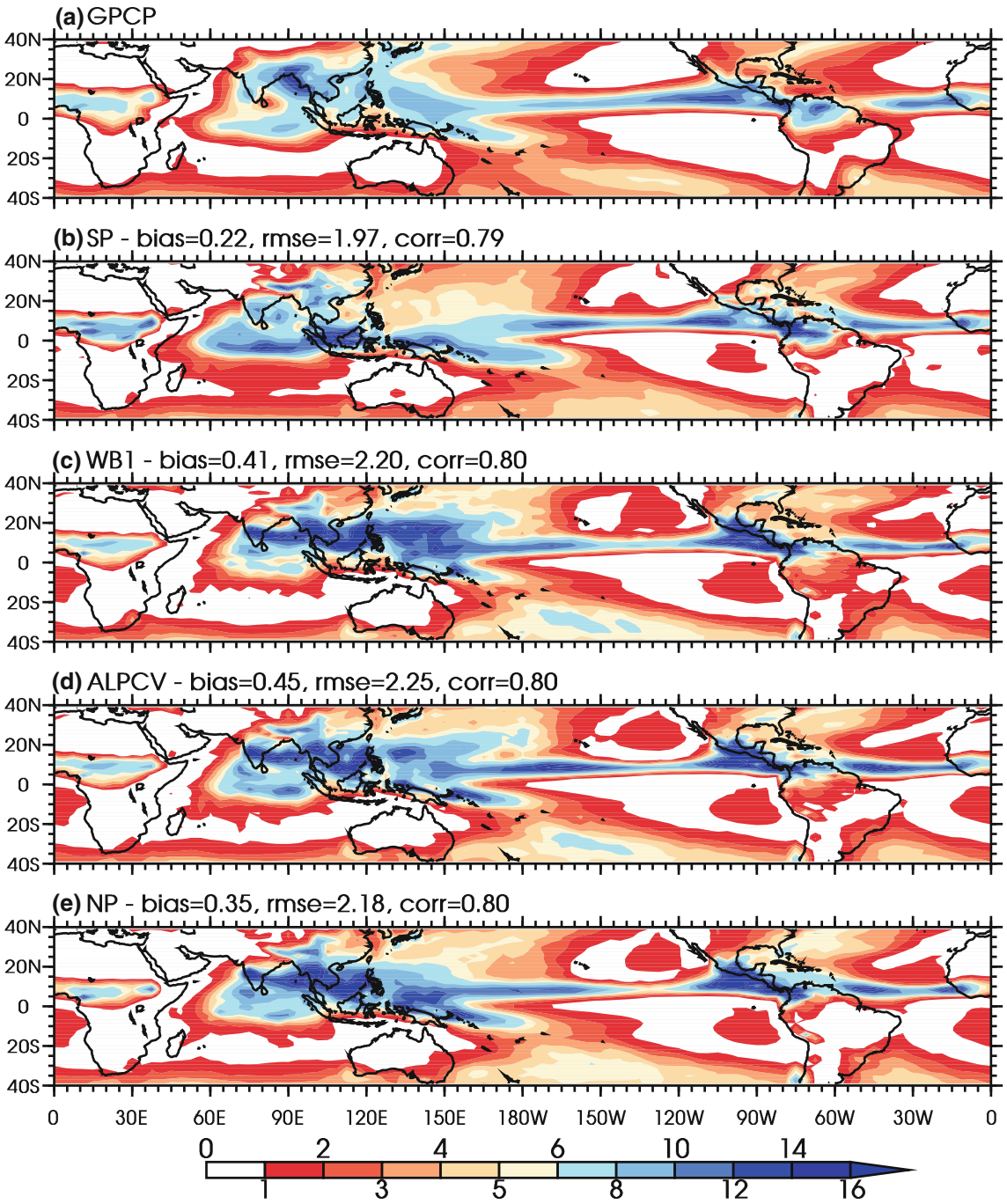

Fig. 15 JJAS mean precipitation (mm day^{-1}) as observed by GPCP and simulated by various versions of the LMDZ model in forced mode: SP, WB1, ALPCV and NP (from *top* to *bottom*). Metrics such as mean bias, correlation coefficient and RMS error between the model and observations (computed on the GCM grid) are indicated for information

LMDZ general circulation model. It breaks away from the more traditional approach consisting of relating deep convection occurrence and intensity directly to mean environmental properties. The so-called ALP closure, based on the computation of a lifting power available at cloud base, requires explicit representation of sub-cloud processes able to lift air for convection. In LMDZ, two new parameterizations of such processes have been developed and implemented: one for boundary-layer thermals and one for evaporatively-driven cold pools. This new set of parameterizations, coupled together via the ALP closure, was shown to improve the representation of the diurnal cycle of continental convection in the mid-latitudes in 1D mode by Rio et al. (2009). From this 1D case study to full

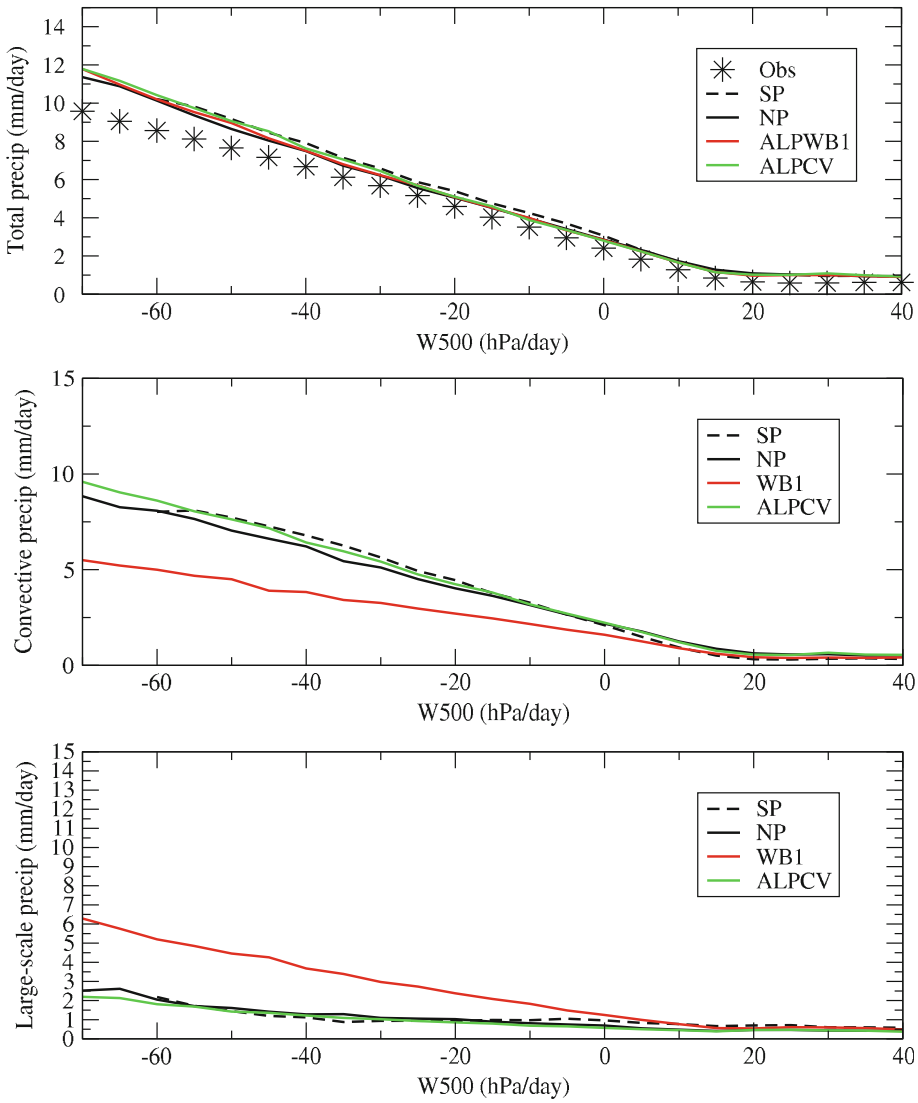

Fig. 16 Total (*top*), convective (*middle*) and large-scale (*bottom*) precipitation (mm day^{-1}) as a function of the dynamical regime at 500 hPa averaged over tropical ocean (30N–30S) as simulated with various versions of the LMDZ model in 3D forced mode: SP (*black dash*), NP (*black*), WB1 (*red*), ALPCV (*green*). Total precipitation is compared with observations from GPCP (*black crosses*)

3D simulations the ALP closure had to be revisited however, as it was shown in particular to underestimate the intensity of tropical oceanic convection.

A key aspect of the ALP closure formulation highlighted in this paper relies on the specification of the updraft vertical velocity at the level of free convection. Updraft vertical velocities are known to be stronger over land than over ocean, and also appear to be weaker during active convective periods than during suppressed convective periods over ocean. We thus propose a profile for the updraft vertical velocity increasing with the height of the LFC in the convective region. The profile is quite arbitrary defined but makes the updraft vertical velocity at LFC dependent on environmental conditions, so that it is less than 0.5 m^{-1} during oceanic active convection, close to 1 m s^{-1} during oceanic suppressed convection or mid-latitude continental convection and closer to 2 m s^{-1} in semi-arid conditions. As this velocity defines the power lost by dissipation between LCL and LFC, this allows the reinforcement of convection over ocean, and a larger delay with insolation of the diurnal cycle of continental precipitation in semi-arid than in the mid-latitude conditions. Considering an additional contribution to the lifting power proportional to the low-level convergence also yields more intense precipitation over ocean, but is not able to correctly represent the timing of precipitation in semi-arid regions. The potential contribution from low-level convergence to the lifting was simply estimated here, and probably overestimated, but it could be related to the transport of subgrid w'^2 by the large-scale low-level winds. This will be investigated further in the future.

Further evaluation of the proposed parameterizations coupled together via the ALP closure in an oceanic and a continental case studies shows that mean environmental properties are also better reproduced with the new version of the model. This is due to a better representation of key

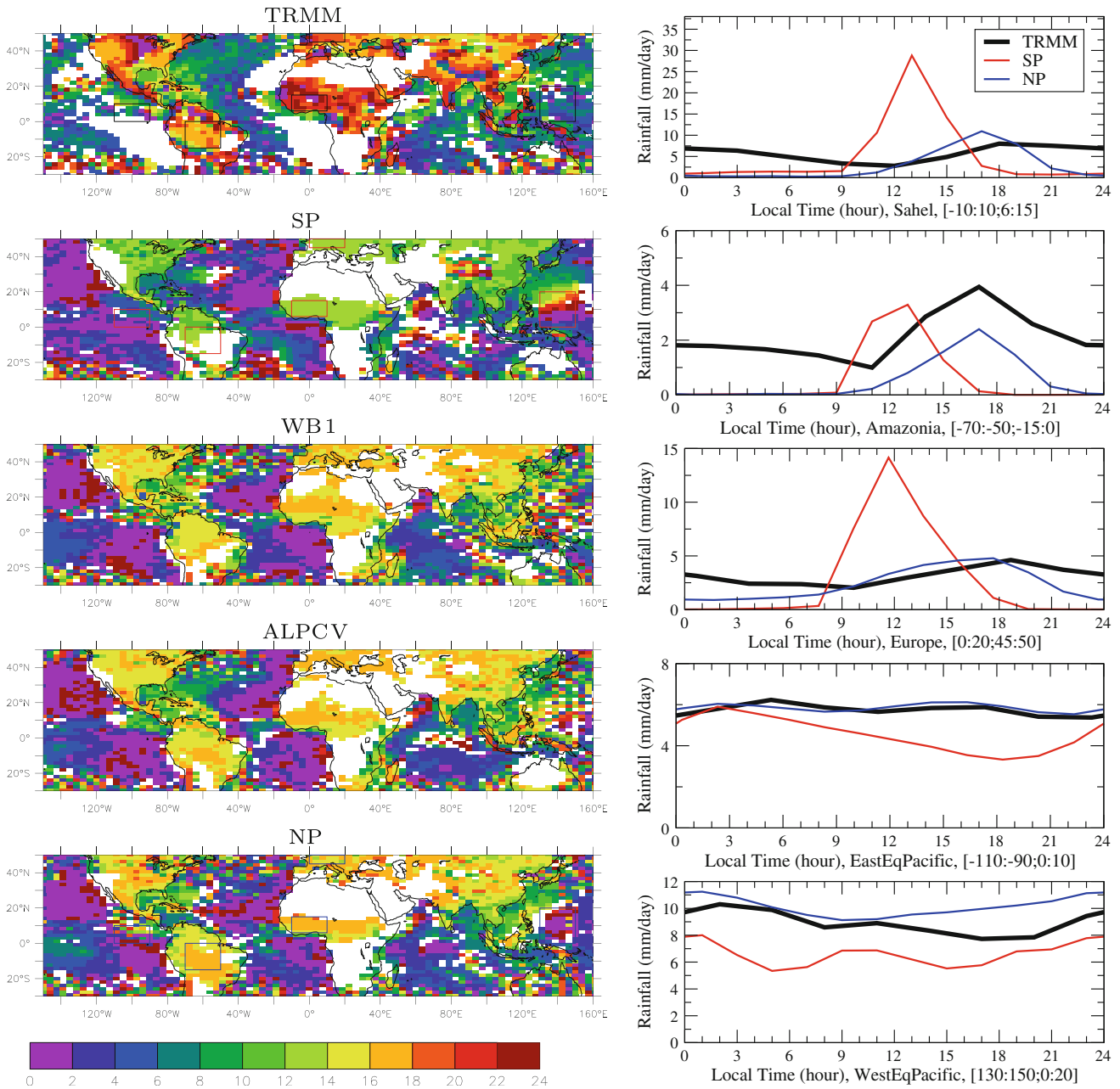

Fig. 17 *Left panel* Local hour of the first harmonic of the diurnal cycle of rainfall as observed by TRMM and as simulated with different versions of the LMDZ model in 3D forced mode: SP, WB1, ALPCV and NP (from *top* to *bottom*). *Right panel* Mean diurnal cycle of precipitation over five specific regions highlighted in the *left panel* (Sahel, Amazon, Europe, East and West Equatorial Pacific) as observed by TRMM and as simulated with SP and NP. Results are averaged over 9 years of simulations and TRMM observations have been projected on the GCM grid

processes modifying in particular the boundary layer: thermals that pre-condition deep convection and cold pools that tend to restabilize low levels. The results highlight in particular the importance of partitioning the total grid cell into the convective region and the cold pool region. It allows deep convection to occur in a more unstable environment associated with weaker convective inhibition during deep convection development, so that convection lasts longer. In addition to a better representation of the presented observed case studies, the new version of the model is also shown to strongly modify the simulation of precipitation in the full GCM. The version of the GCM including the new set of parameterizations exhibits more realistic patterns of global precipitation and also leads to a better representation of the timing of continental convection, as shown here for the Northern

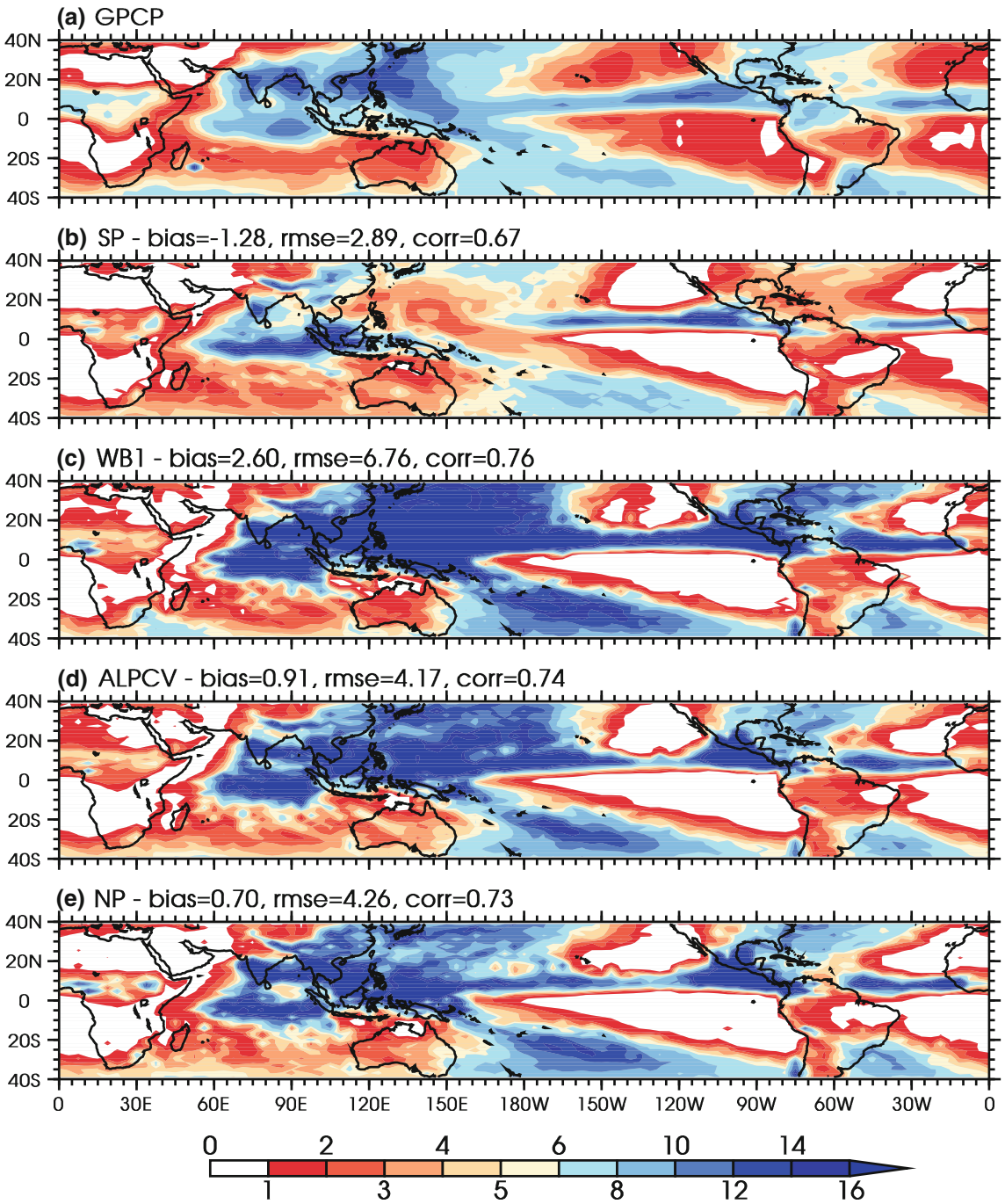

Fig. 18 Standard deviation of JJAS daily rainfall anomalies (mm/day) as observed by GPCP and simulated with different versions of the LMDZ model in 3D forced mode: SP, WB1, ALPCV, NP (from *top* to *bottom*). Daily rainfall anomalies are computed against their mean seasonal cycle. Metrics such as mean bias, correlation coefficient and RMS error between the model and observations (computed on the GCM grid) are indicated for information

Hemisphere summer season. As a result, the intra-seasonal variability of precipitation is also profoundly modified. It now appears to be overestimated, while it was dramatically underestimated in the previous version of the model. How the high-frequency variability impacts lower-frequency variability is a question that needs to be investigated further.

Results also show some deficiencies of the current parameterizations, related to the representation of sub-grid sub-cloud processes. For example, the contribution from shallow cumulus to the mass flux at cloud base, as given by the thermal plume model, is overestimated over ocean. In semi-arid regions on the contrary, thermal activity appears to be underestimated with a weak vertical velocity and

associated third order moment. Aside from improvements in the formulation of the thermal plume model itself, the thermal plume activity should also be partitioned into the convective and the cold pool regions, which may modify thermal activity once cold pools develop. Even if the proposed parameterizations still have shortcomings, the CRM results support the idea of a closure based on sub-cloud processes. Indeed, we find a much stronger link between the cloud-base mass flux and the third-order moment of vertical velocity at LCL, namely the lifting power, than with CAPE. This favors the concept of closures based on lifting power from sub-grid sub-cloud processes rather than mean environmental properties.

It is noteworthy that some fundamental behavior of the model versions on constrained 1D case studies are reproduced in the full 3D version of the model. This is true here for the intensity of convective versus non convective precipitation, or for the local hour of maximum rainfall. The use of 1D case studies to improve parameterizations is thus demonstrated to be relevant for improving the 3D atmospheric models.

Even if significant progress has been made in the physical representation of convective processes, the underestimation of the strongest convective events of the active monsoon phase of TWP-ICE in the standard as in the new versions of the model suggests that processes are still mis-represented independently of the CAPE or ALP closures. This could be related to the underestimation of entrainment, a well-known difficulty for deep convection parameterizations (Derbyshire et al. 2004). The effect of gust front on surface fluxes also deserves to be addressed and parameterized, as it also plays a key role in the life cycle of convective systems (Redelsperger et al. 2000). Even more importantly, the degree of organization of convection in relation with cold pools and anvil activity should be addressed in further details. Only few general circulation models include a representation of cold pools (Grandpeix and Lafore 2010) or mesoscale updrafts and downdrafts within mesoscale convective systems (Donner 1993). However, the mesoscale organization of convection is probably the next challenge to be addressed for general circulation models (Del Genio 2011).

References

Ackerman A, Toon O, Stevens D, Heymsfield A, Ramanathan V, Welton E (2000) Reduction of tropical cloudiness by soot. Science 288:1042

Arakawa A, Chen JM (1987) Closure assumptions in the cumulus parameterization problem. Collection of papers at symposium of short- and medium range numerical prediction, Tokyo, Japan, WMO/IUGG NWP

Arakawa RA, Schubert WH (1974) Interaction of a cumulus cloud ensemble with the large scale environment. part I. J Atmos Sci 31:674–701

Bony S, Emanuel KA (2001) A parameterization of the cloudiness associated with cumulus convection; evaluation using TOGA COARE data. J Atmos Sci 58:3158–3183

Bony S, Dufresne JL, Le Treut H, Morcrette JJ, Senior C (2004) On dynamic and thermodynamic components of cloud changes. Clim Dyn 22:71–86

Bretherton C, McCaa J, Grenier H (2004) A new parameterization for shallow cumulus convection and its application to marine subtropical cloud-topped boundary layers. Part I: description and 1D results. Mon Wea Rev 132:864–882

Couvreux F, Hourdin F, Rio C (2010) Resolved versus parameterized boundary-layer plumes. Part I: a parameterization-oriented conditional sampling in large-eddy simulations. Boun Layer Meteor 134(3):441–458

Couvreux F, Rio C, Guichard F, Lothon M, Canut G, Bouniol D, Gounou A (2012) Initiation of local convection in a semi-arid region analyzed with Large-Eddy Simulations and AMMA observations. Q J R Meteorol Soc 138:56–71

Del Genio AD (2011) Representing the sensitivity of convective cloud systems to tropospheric humidity in general circulation models. Surv Geophys. doi:101007/s10712-011-9148-9

Del Genio AD, Yao MS (1993) Efficient cumulus parameterization for long-term climate studies: the GISS scheme. In: The representation of cumulus convection in numerical models, AMS Meteor Monograph KA Emanuel and DA Raymond, Eds, no 46 American Meteorological Society 24:181–184

Derbyshire SH, Beau I, Bechtold P, Gandpeix JY, Piriou JM, Redelsperger JL, Soares P (2004) Sensitivity of moist convection to environmental humidity. Q J R Meteorol Soc 130:3055–3079

Donner L, Phillips VT (2003) Boundary layer control on convective available potential energy: Implications for cumulus parameterizations. J Geophys Res 108. doi:10.1029/2003JD003,773

Donner LJ (1993) A cumulus parametrization including mass-fluxes, vertical momentum dynamics, and mesoscale effects. J Atmos Sci 50:889–906

Emanuel KA (1991) A scheme for representing cumulus convection in large-scale models. J Atmos Sci 48:2313–2335

Emanuel KA, Zivkovic-Rothman M (1999) Development and evaluation of a convection scheme for use in climate models. J Atmos Sci 56:1766–1782

Fridlind AS, Ackerman AM, Chaboureau JP, Fan J, Grabowski WW, Hill A, Jones TR, Khaiyer MM, Liu G, Minnis P, Morrison H, Nguyen L, Park S, Petch JC, Pinty JP, Schumacher C, Shipway B, Varble AC, Wu X, Xie S, Zhang M (2012) A comparison of TWP-ICE observational data with cloud-resolving model results. J Geophys Res 117:D05,204

Grandpeix JY, Lafore JP (2010) A density current parameterization coupled to emanuel's convection scheme. part i: the models. J Atmos Sci 67(4):881–897

Grandpeix JY, Lafore JP, Cheruy F (2010) A density current parameterization coupled to emanuel's convection scheme. part ii: 1d simulations. J Atmos Sci 67(4):898–922

Guichard F, Petch J, Redelsperger J, Bechtold P, Chaboureau J, Cheinet S, Grabowski W, Grenier H, Jones C, Koehler M, Piriou JM, Tailleux R, Tomasini M (2004) Modelling the diurnal cycle of deep precipitating convection over land with cloud-resolving models and single column models. Q J R Meteorol Soc 130:3139–3172

Hourdin F, Couvreux F, Menut L (2002) Parameterisation of the dry convective boundary layer based on a mass flux representation of thermals. J Atmos Sci 59:1105–1123

Hourdin F, Musat I, Bony S, Braconnot P, Codron F, Dufresne JL, Fairhead L, Filiberti MA, Friedlingstein P, Grandpeix JY,

Krinner G, LeVan P, Li ZX, Lott F (2006) The LMDZ4 general circulation model: climate performance and sensitivity to parametrized physics with emphasis on tropical convection. Clim Dyn 27:787–813

Hourdin F, Grandpeix JY, Rio C, Bony S, Jam A, Cheruy F, Rochetin N, Fairhead L, Idelkadi A, Musat I, Dufresne JL, Lefebvre MP, Lahellec A, Roehrig R (2012) From IPSL-CM5A to IPSL-CM5B: revisiting the parameterization of boundary-layer, clouds and convection in the LMDZ atmospheric model. Clim Dyn. doi:10.1007/s00382-012-1343-y

Houze RA, Hobbs PV (1982) Organization and structure of precipitating cloud systems. Adv Geophys 24:225–315

Houze RA (1977) Structure and dynamics of a tropical squall-line system. Mon Wea Rev 105:1540–1567

Huffman GJ, Adler R, Morrissey MM, Bolvin DT, Curtis S, Joyce R, McGavock B, Susskind J (2001) Global precipitation at one degree daily resolution from multisatellite observations. J Hydrometeorol 2:36–50

Jones TR, Randall DA (2011) Quantifying the limits of convective parameterizations. J Geophys Res 106:D08,210. doi:10.1029/2010JD014913

Jorgensen DP, Lemone MA (1989) Vertical velocity characteristics of oceanic convection. J Atmos Sci 46:621–640

Kuang Z, Bretherton CS (2006) A mass-flux scheme view of a high-resolution simulation of a transition from shallow to deep convection. J Atmos Sci 63:1895–1909

Kummerov C et al. (2001) The evolution of the Goddard profiling algorithm (GPROF) for rainfall estimation from passive microwave sensors. J Appl Met 40:1801–1820

Lafore JP, Stein J, Asencio N, Bougeault P, Ducrocq V, Duron J, Fisher C, Hreil P, Mascart P, Masson V, Pinty JP, Redelsperger JL, Richard E, Vil-Guerau de Arellano J (1998) The Meso-NH atmospheric simulation system. Part I: adiabatic formulation and control simulations. Ann Geophys 16:90–109

Laval K, Sadourny R, Serafini Y (1981) Land surface processes in a simplified general circulation model. Geophys Astrophys Fluid Dyn 17:129–150

LeMone MA, Pennell WT (1976) The relationship of trade wind cumulus distribution to subcloud layer fluxes and structure. Mon Wea Rev 104:524–539

Lemone MA, Zipser EJ (1980) Cumulonimbus vertical velocity events in GATE. Part I: diameter, intensity and mass-flux. J Atmos Sci 37:2444–2457

Lima MA, Wilson JW (2008) Convective storm initiation in a moist tropical environment. Mon Wea Rev 136:1847–1864

Lothon M, Campistron B, Chong M, Couvreux F, Guichard F, Rio C, Williams E (2011) Life cycle of a mesoscale circular gust front observed by a C-band Doppler radar in West Africa. Mon Wea Rev 139:1370–1388

Lucas C, Zipser EJ, Lemone MA (1994) Vertical velocity in oceanic convection off Tropical Australia. J Atmos Sci 51:3183–3193

Mapes B (2000) Convective inhibition, subgrid-scale triggering energy, and stratiform instability in a toy tropical wave model. J Atmos Sci 57:1515–1535

Moncrieff MW, Miller MJ (1976) The dynamics and simulation of tropical cumulonimbus and squall lines. Q J R Meteorol Soc 102:373–394

Qian L, Young GS, Frank WM (1998) A convective wake parameterization scheme for use in general circulation models. Mon Wea Rev 126:456–469

Redelsperger JL, Guichard F, Mondon S (2000) A parameterization of mesoscale enhancement of surface fluxes for large-scale models. J Clim 13:402–421

Rio C, Hourdin F (2008) A thermal plume model for the convective boundary layer: representation of cumulus clouds. J Atmos Sci 65:407–425

Rio C, Hourdin F, Grandpeix JY, Lafore JP (2009) Shifting the diurnal cycle of parameterized deep convection over land. Geophys Res Lett 36:L07,809. doi:10.1029/2008GL036779

Rio C, Hourdin F, Couvreux F, Jam A (2010) Resolved versus parameterized boundary-layer plumes. Part II: continuous formulations of mixing rates for mass-flux schemes. Boun Layer Meteor 135:469–483

Rozbicki JJ, Young G, Qian L (1999) Test of a convective wake parameterization in the single column version of CCM3. Mon Wea Rev 127:1347–1361

Steiner M, Houze R, Yuter SE (1995) Climatological characterization of three-dimensional storm structure from operational radar and rain gauge data. J Appl Met 34:1978–2007

Stevens DE, Ackerman AS, Bretherton CS (2002) Effects of domain size and numerical resolution on the simulation of shallow cumulus convection. J Atmos Sci 59:3285–3301

Taylor KE, Stouffer RJ, A MG (2012) An overview of CMIP5 and the experiment design. Bull Am Meteorol Soc 93:485–498

Tiedtke M (1989) A comprehensive mass flux scheme for cumulus parameterization in large-scale models. Mon Wea Rev 117:1179–1800

Varble AM, Fridlind A, Zipser EJ, Ackerman AS, Chaboureau JP, Fan J, Hill A, McFarlane SA, Pinty JP, Shipway B (2011) Evaluation of cloud-resolving model intercomparison simulations using TWP-ICE observations: precipitation and cloud structure. J Geophys Res 116:D12,206

Xie S, Hume T, Jakob C, Klein S, Mccoy R, Zhang M (2010) Observed large-scale structures and diabatic heating and drying profiles during TWP-ICE. J Clim 23:57–79

Xu KM, Randall DA (2000) Updraft and downdraft statistics of simulated tropical and midlatitude cumulus convection. J Atmos Sci 58:1630–1649

Yamada T (1983) Simulations of nocturnal drainage flows by a q^2l turbulence closure model. J Atmos Sci 40:91–106

Zhu P, Dudhia J, Field PR, Wapler K, Fridlind A, Varble A, Zipser E, Petch J, Chen M, Zhu Z (2012) A limited area model (LAM) intercomparison study of a TWP-ICE active monsoon mesoscale convective event (submitted to JGR)

Zipser EJ (1969) The role of organized unsaturated convective downdrafts in the structure and rapid decay of an equatorial disturbance. J Appl Met 8:799–814

Zipser EJ, Lemone MA (1980) Cumulonimbus vertical velocity events in GATE. Part II: synthesis and model core structure. J Atmos Sci 37:2458–2469